

**FIRST-PRINCIPLES STATISTICAL MECHANICS
OF SEMICONDUCTOR ALLOYS AND INTERMETALLIC COMPOUNDS**

Alex Zunger

National Renewable Energy Laboratory
Golden, Colorado 80401, USA

ABSTRACT

A binary substitutional system can exist in 2^N configurations that can be formed by occupying any of the N sites of a lattice by either an A or a B atom. Substitutional configurations include compounds, alloys, superlattices, and substitutional impurities. This article addresses the questions of (i) finding the lowest energy configuration of a given A/B substitutional system, (ii) calculating its composition-temperature phase diagram, and (iii) its finite-temperature thermodynamic properties, using the first-principles local density approximation (LDA). Mapping of the LDA energies of 10-20 A_pB_q compounds onto an Ising-like "cluster expansion" enables use of lattice statistical mechanics techniques that elegantly solve the above problems. This extends the utility of the LDA from simple, perfectly-ordered compounds to truly complex structures. We illustrate the method for semiconductor systems and transition-metal intermetallic systems, emphasizing the role of lattice relaxation.

Submitted to the Proceedings of the NATO ASI on "Statics and Dynamics of Alloy Phase Transformations," Plenum Press (1993).

I. INTRODUCTION

Many important solid-state structures can be described as substitutional A/B systems, in which the sites of a crystal lattice are occupied by A and B atoms in different patterns ("configurations"). These include abrupt and intermixed superlattices, substitutional impurities, impurity aggregates, ordered A_pB_q superlattices, and random $A_{1-x}B_x$ alloys. In theoretical studies of the energetics of substitutional systems it is often necessary to find the ground-state configuration for a given lattice type, or to calculate finite-temperature thermodynamic averages. These applications require, in principle, sampling of the 2^N possible configurations for placing A and B atoms on N lattice sites. This presents a major challenge since (i) the number of possible configurations increases exponentially with the number of lattice sites N and (ii) it may be necessary to calculate the energy of configurations with many atoms. Since the computational effort for quantum-mechanical total-energy calculations increases rapidly with the number of atoms in the unit cell, direct first-principles studies are usually limited to a small subset of the configuration space, i.e., about 10-20 structures with ≤ 50 atoms per cell out of a total of 2^N configurations. To find the stable crystal structures in such restricted first-principles total energy approaches [1] one usually repeats the total energy calculation for a few assumed crystal structures that by analogy with related compounds or by "chemical intuition" are expected to be likely competitors for the stable ground state. Comparison of total energy vs volume curves for such a set of "intuitive structures" permits the identification of the stablest structure in this set. While generally successful [1], the predictive value of this approach of "rounding up the usual suspects" does depend on one's ability to guess at the outset a set of structures which includes the "winning" (minimum energy) configuration. One wonders, however, if a different, hitherto unsuspected structure could have yet lower energy, or whether a linear combination of two other structures could have a lower energy. Addressing this problem, even for binary A_pB_q compounds requires, in principle, calculation of the total energies of the 2^N atomic configurations for each type of lattice (fcc, bcc...). Even limiting N to ~ 40 sites, this is a formidable task for first-principles electronic structure methods [1], as it involves an astronomical number of calculations (of the order of the number of stars in this galaxy). This problem can be circumvented to some extent by using simplified electronic Hamiltonians (e.g., minimal basis set tight binding) in conjunction with perturbation theory [2] or by replacing the quantum mechanical total energy by phenomenological effective pair potentials [3]. These approaches, however, have limited accuracy and only work for specialized cases. It is the purpose of this article to demonstrate how one can

effectively (i) perform such a ground state search among many atomic configurations and, (ii) obtain the temperature-composition phase diagram in a *first-principles manner*, using directly calculated (local density [1]) total energies of only ~ 10-20 configurations.

II. REAL SPACE CLUSTER EXPANSIONS

A general approach to the energetics of substitutional systems is the Cluster Expansion (CE) [4-8], in which the energies of the different configurations are described by a generalized Ising Hamiltonian. In the cluster expansion, the alloy is treated as a lattice problem: One uses a given underlying lattice (fcc, bcc, etc.) and defines a configuration σ by specifying the occupation of each of the N lattice sites by an A atom or a B atom. For each configuration, one assigns a set of fictitious "spin" variables \hat{S}_i ($i = 1, 2, \dots, N$) to each of the N sites of the lattice, with $\hat{S}_i = -1$ if site i is occupied by an A atom, and $\hat{S}_i = +1$ if it is occupied by a B atom. The set of spin variables $\{\hat{S}_i\}$ defines the configuration, σ . One can imagine that the total electronic + nuclear energy of a given configuration σ can be calculated directly (in principle, quantum mechanically), yielding $E_{\text{direct}}(\sigma) = \langle \Psi | H | \Psi \rangle / \langle \Psi | \Psi \rangle$. In principle, this can be repeated for each σ . The cluster expansion consists of mapping the set $\{E_{\text{direct}}(\sigma)\}$ onto an Ising-like series. In fact, for a lattice with N sites, the problem of finding the energies of the 2^N possible configurations can be *exactly* [9] mapped into the Hamiltonian:

$$E_{\text{CE}}(\sigma) = J_0 + \sum_i J_i \hat{S}_i(\sigma) + \sum_{j < i} J_{ij} \hat{S}_i(\sigma) \hat{S}_j(\sigma) + \sum_{k < j < i} J_{ijk} \hat{S}_i(\sigma) \hat{S}_j(\sigma) \hat{S}_k(\sigma) + \dots, \quad (1)$$

for configuration σ , where the J 's are "interaction energies", and the first summation is over all sites in the lattice, the second over all pairs of sites, the third over all triplets, and so on. These constitute the basic "figures" of the lattice, illustrated for the fcc lattice in Fig. 1. The interaction energies, $\{J\}$, are the same for all configurations σ . Thus, if the J 's are known, the energy $E_{\text{CE}}(\sigma)$ of any configuration can be calculated almost immediately by simply calculating the spin products and summing Eq. (1). Because the Ising representation of the energy can be calculated rapidly, and is also a linear function of the spin products, one can readily (i) apply linear programming techniques to find ground state structures (e.g., Ref. [10]), (ii) use statistical mechanics techniques such as the Cluster Variation Method [11] or Monte Carlo [12] to calculate phase diagrams, and (iii) calculate the energy of an arbitrarily complex configuration [13].

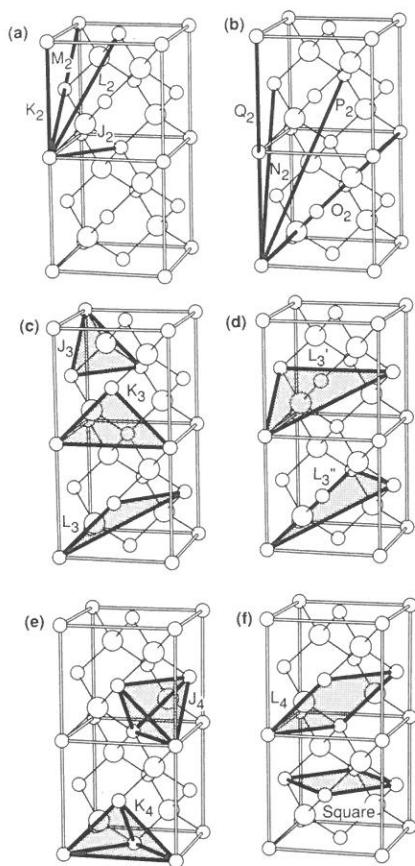


Figure 1. Atomic figures used in the cluster expansion. (a) and (b) show pair figures; (c) and (d) show 3-body figures; and (e) and (f) show 4-body figures.

σ , the resulting configuration is "relaxed". We see that one can construct a cluster expansion for the 2^N unrelaxed energies (thus defining a set of 2^N unrelaxed J 's), or construct an expansion for the 2^N relaxed energies (thus defining a set of 2^N relaxed J 's). In either case, the orthonormality and completeness of the set of spin products guarantees [14] that the mapping of $\{E_{\text{direct}}(\sigma)\}$ onto $\{E_{\text{CE}}(\sigma)\}$ exists.*

We can define a correlation function, $\bar{\Pi}_F$ for each class of symmetry-equivalent figures, F , as the average for each configuration of the spin products over all figures that make up F :

*The assertion of Xi, Chakraborty, Jacobsen, and Norskov [14] that $E_{\text{CE}}(\sigma)$ cannot, in principle, represent such a $E_{\text{direct}}(\sigma, \{\vec{R}_i\})$, is, hence, false. Note, however, that in our representation $\{\vec{R}_i\}$ is fixed for each σ (either at the unrelaxed or at the relaxed values) and does not take random values. Hence, vibrational entropy is not included in the form of Eq. (1). Vibrational entropy can be added as a separate term.

The Hamiltonian of Eq. (1) contains 2^N interaction energies J , which are used to describe the energies of the 2^N configurations σ . Consequently, Eq. (1) can be viewed as defining a set of linear equations, in which a $2^N \times 2^N$ matrix of spin products multiplies a 2^N vector of J 's, giving a vector of the energies of the 2^N configurations. Viewed this way, it is obvious that the J 's of Eq. (1) can be solved for exactly if the matrix of spin products is nonsingular. Actually, Sanchez et al. [9] have proven that the matrix is orthonormal which guarantees that Eq. (1) is always solvable.

The directly calculated energy $E_{\text{direct}}(\sigma)$ depends in general on the $3N-3$ atomic positions \vec{R}_i . If these are restricted to the ideal lattice positions, we term the corresponding configuration as "unrelaxed", while if $\{\vec{R}_i\}$ are optimized to yield the minimum $E_{\text{direct}}(\sigma)$ of a given

$$\bar{\Pi}_F(\sigma) = \frac{1}{ND_F} \sum_f \hat{S}_{i_1}(\sigma) \hat{S}_{i_2}(\sigma) \dots \hat{S}_{i_m}(\sigma) , \quad (2)$$

where f run over the ND_F figures in class F , the spin indices run over the m sites of figure f , and D_F is the number of figures of class F per site. We can now rewrite Eq. (1) as

$$E_{CE}(\sigma) = N \sum_F D_F J_F \bar{\Pi}_F(\sigma) , \quad (3a)$$

for a particular configuration σ , and

$$\langle E_{CE} \rangle = N \sum_F D_F J_F \langle \bar{\Pi}_F \rangle \quad (4)$$

for the configuration-averaged disordered alloy. Here, D_F is the number of figures of class F per site. We see that the problem breaks naturally into two parts: (a) "Energetics", i.e., calculation of the interaction energies $\{J_F\}$ from some microscopic Hamiltonian, and, (b) "Statistics", i.e., solving Eq. (4) with a given set $\{J_F\}$, thus finding the ground state ($T=0$) stable configurations out of 2^N possibilities [10], and obtaining finite-temperature phase diagrams [11,12].

When the CE converges rapidly, the energies of the 2^N configurations are approximately linearly dependent. In this case, knowing a few of the energies allows us to determine the rest. Thus the advantage of the cluster expansion is that it extracts information from a small set of structures to make predictions for the energies of all other structures; by contrast, direct electronic structure calculations [1] treat each configuration independently, and fail to take advantage of the underlying relations among different substitutional configurations of the system.

To summarize, the CE of Eq. (1) constitutes an exact mapping of either relaxed or unrelaxed energies of a nonvibrating lattice onto an Ising series. If a practically converged form can be established, it can be used to scan the 2^N configuration space searching for "ground state structures". In conjunction with the CVM or MC, it can be used to calculate phase diagrams. We next discuss how the interaction energies might be determined.

III. ENERGETICS: DETERMINATION OF INTERACTION PARAMETERS IN THE CLUSTER EXPANSION

There are three general approaches to this problem.

The first approach is to do a purely empirical fit of the J 's to known features of the phase diagram for the alloy system [15-16]. For example, information about the values of the J 's

may be extracted from experimental critical temperatures. This approach is the simplest, but it requires an intrinsically unverifiable truncation to a small number of J 's, and provides little new information about the properties of the alloy. Furthermore, it was shown [17] that for systems with size-mismatched A and B atoms the J 's extracted from fitting experimental critical temperatures fail to reproduce the observed mixing enthalpies.

The second approach is to determine the J 's by treating ordered structures as perturbations of the random alloy. The random alloy is treated using either the Virtual Crystal Approximation (VCA) [18] or the Coherent Potential Approximation (CPA) [19-23], and the electronic band structure is treated with the Tight-Binding (TB) method [19-21] or the Korringa, Kohn, and Rostoker (KKR) method [22,23]. Methods based on these approaches include the Generalized Perturbation Method (GPM) of Ducastelle [19], the Concentration-Wave (CW) method of Gyorfyy et al. [22,23], and the Linear Response Theory (LRT) [18]. In the latter case the random alloy is treated by applying the VCA within the pseudopotential method. The interaction energies are then calculated using first order perturbation theory, where the difference between the atomic pseudopotentials is the perturbation. This method provides accurate, first-principles results, but it is limited to alloys in which the atomic species are similar enough for first-order perturbation theory to work, and is only practical for calculating pair interaction energies. The CPA-based mean-field methods—GPM and CW—currently neglect both positional fluctuations (relaxations) and charge fluctuations. I will return to this point in Sections IV and IX.

The third approach is the direct inversion method of Connolly and Williams [7,8,17,24-32]. In this method, N_σ configurations are selected for direct electronic structure calculations. The excess energy of a configuration σ with composition $A_{1-x}B_x$ at volume V is defined by

$$\Delta E(\sigma, V) = E(\sigma, V) - [(1 - x)E(A, V_A) + xE(B, V_B)] \quad (5)$$

where $E(A, V_A)$ and $E(B, V_B)$ are the energies of pure A and B solids at their equilibrium volumes V_A and V_B . The directly calculated formation enthalpy is defined by

$$E_{\text{direct}}(\sigma) = \Delta H(\sigma) = \Delta E(\sigma, V_\sigma) = \min_V \Delta E(\sigma, V), \quad (6)$$

where V_σ is the equilibrium volume of configuration σ and all structural degrees of freedom are relaxed. One selects N_σ structures and N_F figures, with $N_F \leq N_\sigma$, such that the cluster expansion of Eq. (3a) is converged when the sum is restricted to these N_F figures. The correlation functions and the calculated energies for these configurations are then used to fit

the interaction energies of Eq. (4), by solving

$$\sum_{\sigma}^{N_{\sigma}} \omega_{\sigma} |E_{\text{direct}}(\sigma) - N \sum_{\text{F}}^{N_{\text{F}}} D_{\text{F}} J_{\text{F}} \bar{\Pi}_{\text{F}}(\sigma)|^2 = \text{Minimum} , \quad (7)$$

with respect to the N_{F} values of J_{F} , where ω_{σ} are weights. Equation (7) can be solved using the singular value decomposition technique [33]. For the special case of $N_{\sigma} = N_{\text{F}}$ (which is the case used by Connolly and Williams [7], we can solve explicitly for the J 's in terms of the E 's:

$$D_{\text{F}} J_{\text{F}} = \sum_{\sigma'} [\bar{\Pi}_{\text{F}}(\sigma')]^{-1} E_{\text{direct}}(\sigma') . \quad (8)$$

A few comments are pertinent here:

(i) Equation (8) highlights the differences between the CE and the conventional interatomic potentials approach [3]. In the latter, E_{direct} is written as a sum of two-body (V_{ij}), three-body (V_{ijk}), and higher potentials, so that Eq. (8) becomes

$$D_{\text{F}} J_{\text{F}} = \sum_{\sigma'} [\bar{\Pi}_{\text{F}}(\sigma')]^{-1} \left[\sum_{ij}^{\infty} V_{ij} + \sum_{ijk}^{\infty} V_{ijk} + \dots \right] . \quad (9)$$

Thus, each J_{F} in the CE method renormalizes in it all interatomic potentials (two-body, three-body, etc., summed over all interatomic distances), so that even the $J_{\text{F}} =$ nearest-neighbor pair interaction of the CE contains information from *all* interatomic potentials at this volume. We thus sometimes refer to this CE method as the "renormalized interaction" approach.

(ii) Equation (8) clarifies the point that a "figure" F should not be interpreted geometrically, but rather topologically: its energy J_{F} corresponds to a sum over configuration, each having differently relaxed geometries for the same figure.

(iii) One hears sometimes the question "how can interaction energies deduced from a set of *ordered* configurations [Eq. (8)] be used to describe *random* alloys [Eq. (4)], given that the two phases are known to sometimes have very different physical properties?" The formal answer goes back to the fact that the untruncated Eq. (1) is exact [9]. The *only* source of error in practical applications is its truncation. Hence, it is imperative that one examines quantitatively truncation errors. If this is satisfied to a given tolerance, the energy of *any* configuration σ can be expressed as a linear combination of the energies of other configurations $\{\sigma'\}$, as can be verified by inserting Eq. (8) into Eq. (3a):

$$E_{\text{CE}}(\sigma) = N \sum_{\sigma'} A(\sigma, \sigma') E(\sigma') \quad (3b)$$

with

$$A(\sigma, \sigma') = \sum_{\mathbf{F}} \bar{\Pi}_{\mathbf{F}}(\sigma) [\bar{\Pi}_{\mathbf{F}}(\sigma')]^{-1}. \quad (3c)$$

(iv) The inversion method provides a direct link between electronic structure and phase stability. The basic structure of the method involves definition of an electronic Hamiltonian \hat{H} (e.g., LDA) used to directly calculate total energies $\{E_{\text{direct}}(\sigma)\}$ of some configurations. These are then used via Eq. (7) to obtain interaction energies $\{J_{\mathbf{F}}\}$ which can be used to perform a ground state search and phase diagram calculations. Schematically

$$\hat{H} \rightarrow \{E_{\text{direct}}(\sigma)\} \rightarrow \{J_{\mathbf{F}}\} \rightarrow \begin{array}{l} \text{ground state search} \\ \text{thermodynamics} \\ \text{phase diagrams.} \end{array} \quad (3d)$$

It is possible to repeat this sequence in "computer experiments" using constrained Hamiltonians \hat{H} , e.g., nonrelativistic vs relativistic; self-consistent vs frozen charge; relaxed vs unrelaxed; s-d hybridized vs nonhybridized and zero pressure vs finite pressure. The corresponding $\{J_{\mathbf{F}}\}$ will naturally reflect these changes, as will the phase diagram. This allows us to study how the classic metallurgical constructs of "size", "charge-transfer", "band structure effects", etc., affect phase stability. This will be illustrated in Sec. VII.

The advantages of the renormalized interaction approach are that it can be applied to a wide class of alloy systems, including both intermetallic and semiconductor alloys, and—when combined with *ab initio* total-energy methods—can provide accurate first-principles results. Since only total energies of ordered compounds are needed as input, one can readily use the well-developed band-theoretic methods which solve the LDA equations highly accurately. In particular, self-consistency, exchange and correlation effects, use of full-potentials, converged total energy expressions and relativistic effects are included. This method can also be used for cluster expansions of other calculated properties besides total energies, such as band gaps [32], bond lengths [8b], and molar volumes [28]. The disadvantage of the method is that convergence must be carefully examined. Clearly, the utility of this approach depends on its rate of convergence. Mathematical completeness requires that 2^N interaction energies be used to describe 2^N configurations. Were we to stop here, the cluster expansion would be completely worthless, since calculating the 2^N J's is as hard as calculating the energies of the 2^N configurations. However, intuition suggests that interactions between distant sites are less important than those between near sites, and that interactions that involve many sites are less important than those that involve fewer sites (see Fig. 1). Thus the number of J's needed in practice may be much smaller than 2^N . If this is

the case, then one can determine the J 's from the energies of a small set of configurations $\{\sigma'\}$ [Eq. (8)] whose energies are calculated directly (independently of the CE, e.g., by first-principles total-energy methods). These J 's can then be used in Eqs. (3b)-(3c) to predict the energies of new configurations $\{\sigma\}$. The quality of the CE is determined by comparing the energies $E_{CE}(\sigma)$ for configurations $\{\sigma\}$ determined by the CE with the energies $E_{direct}(\sigma)$ determined by a direct calculation [8,13,28-32]. If necessary, one can repeat this procedure by adding extra J 's until the predicted energies for $\{\sigma\}$ are smaller than some prescribed tolerance. Two recent examples of such tests were performed for the Madelung energies on an fcc lattice (using the Ewald summation technique for the direct calculations) [31] and for the energies of AlAs/GaAs on a zinc-blende lattice (where the direct calculations were done using local-density total energy calculations) [13]. In both cases, direct calculations for a few (~ 10) simple, ordered structures defined a CE that can predict the remaining configurations with a precision comparable to that of the direct calculations. We next illustrate the convergence of the Ising series in these cases.

IV. CONVERGENCE OF THE CLUSTER EXPANSION: THE ELECTROSTATIC ENERGY OF AN fcc LATTICE WITH POINT CHARGES

A. The Problem

Consider the classic Madelung problem of a simple lattice (e.g., fcc) with $N \rightarrow \infty$ sites labeled $i = 1, 2, \dots, N$, each bearing a net charge Q_i and occupied either by an A atom or by a B atom. Each of the 2^N possible lattice configurations σ has a Madelung energy $E_M(\sigma)$ per atom. It can be expressed as an Hamiltonian with infinite range interactions

$$E_M(\sigma) = \frac{1}{2N} \sum'_{i,j} \frac{Q_i Q_j}{|R_i - R_j|} = \frac{1}{2N} \sum'_{i,j} \hat{S}_i \hat{S}_j \tilde{J}_{ij}, \quad (10)$$

where the prime excludes the $i=j$ term, and \tilde{J}_{ij} denotes the bare Coulomb interaction energy

$$\tilde{J}_{ij} = \frac{Q_i Q_j}{|R_i - R_j|} \hat{S}_i \hat{S}_j, \quad (11)$$

between charge Q_i on lattice site \vec{R}_i and Q_j on \vec{R}_j . We wish to calculate for the fcc lattice (a) the configuration σ_{min} with the lowest Madelung energy (out of 2^N possibilities), and (b) the energy of a *random* Madelung lattice $A_{1-x}B_x$ as a function of composition x . We will

first find exact analytic solutions and then, independently solve the problem by using a truncated cluster expansion, thus providing insights into its rate of convergence.

B. Modeling Charges on Sites

Before proceeding, we need to construct a simple, yet physically reasonable model for the distribution of point charges Q_i on the sites i . To develop intuition, consider an arbitrary configuration where each of the N sites are occupied by A or B atoms (e.g., Na and Cl) by a coin-flip. When a Na site is surrounded locally mostly by Na atoms, its effective charge would be close to zero, much like in a Na metal; on the other hand, when a Na atom is locally surrounded by Cl atoms, its charge will be closer to +1, much like in NaCl. It hence makes sense to assume that the charge on site i depends in some fashion on the number of *unlike atoms* surrounding it. That this is physically reasonable follows from the existence of a rather short Thomas-Fermi screening length in solids. That this is also numerically valid follows from computer experiments: Figure 2 shows the linear augmented plane wave (LAPW) calculated charge transfer (i.e., atomic charge in a compound relative to the charge in the fcc solids) in supercell models of $\text{Cu}_{0.75}\text{Au}_{0.25}$, $\text{Cu}_{0.75}\text{Pd}_{0.25}$, and $\text{Cu}_{0.5}\text{Pd}_{0.5}$. These supercells were selected to contain a *variety* of local arrangements of atoms about a given site (e.g., in $\text{Cu}_{0.5}\text{Pd}_{0.5}$ we have Pd atoms surrounded by 2,5,7, and 8 Pd nearest neighbors). We see from Fig. 2 that the charge on a given site depends (essentially linearly) on the number of unlike atoms in the first coordination shell.* (This is hardly surprising: Indeed the essence of structural chemistry is that the properties of atomic sites depend on their local chemical environments.)

We hence model the net charge Q_i to be proportional to the number of atoms of *opposite* type in the first coordination shell (containing Z atoms):

$$Q_i = \lambda \sum_{k=1}^Z [\hat{S}_i - \hat{S}_k^{(i+1)}], \quad (12)$$

where \hat{S}_i is the spin on site i , $\hat{S}_k^{(i+1)}$ is the spin on one of the Z atoms that are nearest-neighbors to site i , and λ is a scaling constant determining the maximum charge transfer ($2Z\lambda$). The charge distribution of Eq. (12) has the following properties: (i) the charges on

*In an antiferromagnetic alloy local magnetic moments on a given site also depend almost linearly on the number of nearest sites with an opposite moment.

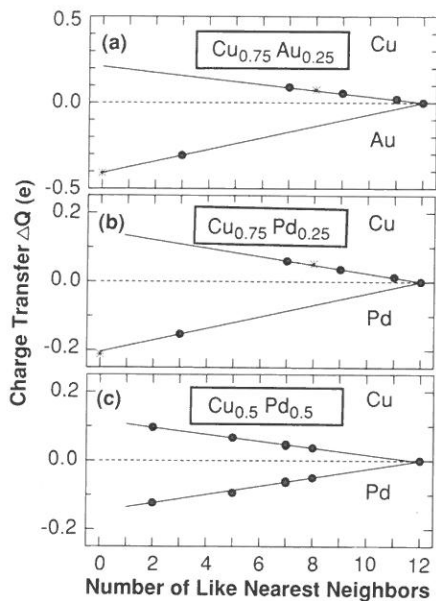


Figure 2. Integrated total-charge transfer inside the muffin-tin spheres of unrelaxed (a) $\text{Cu}_{0.75}\text{Au}_{0.25}$, (b) $\text{Cu}_{0.75}\text{Pd}_{0.25}$ and (c) $\text{Cu}_{0.5}\text{Pd}_{0.5}$ with respect to the pure fcc solids as a function of the number of like atoms in the first coordination shell. The asterisks denote values for the atoms in the ordered L_{12} structure. From ref [30].

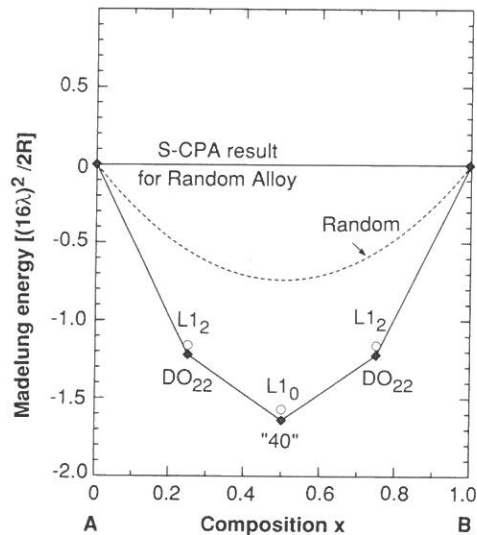


Figure 3. Calculated ground state structures (diamond shaped symbols) of the binary fcc Madelung lattice with charge distribution given by Eq. (12). Open circles denote E_M of unstable structures. The dashed line gives the energy of the random alloy in this model, while the horizontal solid line gives the energy of the random alloy within the S-CPA. From Ref. [31].

A's and B's have opposite signs; (ii) different A sites (and different B sites) can have different charges reflecting variations in the local atomic arrangements; (iii) electro-neutrality $\sum_i Q_i = 0$ is satisfied; (iv) E_M of Eq. (10) is symmetrical with respect to the $A \leftrightarrow B$ replacement; and (v) this definition reduces to the standard definitions of the Madelung energy for AB ordered lattices. Note that the model of Eq. (12) is used only to illustrate convergence effects in the CE method. Actual calculations described in Sec. V and onwards do not involve any model for Q_i , but use instead the continuous electronic charge density $\rho(\vec{r})$.

The physical consideration discussed above are absent in applications of the site coherent potential approximation (S-CPA) to phase stability. There, one postulates [19-23,34a] that in an arbitrary configuration the effective medium potential V_i and charge Q_i on site i do not depend on the environment of i : At a given composition, all A atoms are assumed to have the same charge (and so do all B atoms). It follows from the postulated absence of correlations that the configuration average $\langle Q_i Q_j \rangle$ for the random alloy [Eq. (4)] factors into the product $\langle Q_i \rangle \langle Q_j \rangle$ which is zero, on account of global charge neutrality. Hence, in the

S-CPA we have $\langle E_M \rangle \equiv 0$, i.e., the random alloy carries no electrostatic energy (Fig. 3). This is unphysical. The definition of randomness rests on the absence of correlations between *site occupations*, i.e., $\langle \hat{S}_i \hat{S}_j \rangle = \langle \hat{S}_i \rangle \langle \hat{S}_j \rangle$. The fallacy in the S-CPA is that it assumes that this absence of correlations can also be used for *other* site-related properties, e.g., for the charge on a site, the diagonal tight-binding Hamiltonian element, etc. However, $\langle Q_i Q_j \rangle = \langle Q_i \rangle \langle Q_j \rangle$ does not follow from $\langle \hat{S}_i \hat{S}_j \rangle = \langle \hat{S}_i \rangle \langle \hat{S}_j \rangle$. Local environment effects were recently discussed in Ref. 34b.

Using Eqs. (10)-(12), the Madelung energy per atom for configuration σ in a fcc structure can be written as

$$E_M(\sigma) = -\alpha_M(\sigma) [(16\lambda)^2/2R] \quad (13)$$

while for the random alloy we have:

$$\langle E_M \rangle_R = -\langle \alpha_M \rangle [(16\lambda)^2/2R],$$

where $\alpha_M(\sigma)$ is the Madelung constant, $R = a\sqrt{2}$ is the nearest-neighbor bond length, and a is the cubic fcc lattice constant. We will display our results in units of $(16\lambda)^2/2R$, where $2Z\lambda$ is the charge transfer in a system in which the A atom is surrounded locally only by (Z) B atoms. λ can be calculated from self-consistent band theory, and is expected to scale with the $\chi_A - \chi_B$ electronegativity difference. Since the S-CPA gives $\langle E_M \rangle_R \equiv 0$ and since in our model $\langle \alpha_M \rangle_R$ will end up being of order unity (see below), the error in the S-CPA scales as $(16\lambda)^2/2R$. I expect that for alloys with appreciable ionicity (e.g., Li-Al, Ni-Al), the currently practiced S-CPA methods (GPM and CW) will fail in reproducing realistic formation energies, mixing enthalpies, and ordering energies.

Having established a model for Q_i , we can now solve the problem posed at the beginning of this section. We start with the analytic solution.

C. Analytic Solutions

The configurational average of the Madelung energy, appropriate to a random alloy is

$$\langle E_M \rangle_R = \frac{1}{2N} \sum_{ij} \frac{\langle Q_i Q_j \rangle_R}{R_{ij}} = \frac{1}{2} \sum_m \frac{\langle Q_i Q_{i+m} \rangle_R}{R_m} Z_m, \quad (14)$$

where Q_{i+m} is the charge on an atom in the m th shell (containing Z_m atoms) about the origin at i and R_m is the distance to the origin. Substituting our model (12) for the distribution of point charges into Eq. (14) gives

$$\langle E_M \rangle_R = \frac{\lambda^2}{2} \sum_{m=1}^{\infty} \frac{Z_m}{R_m} F_m(x), \quad (15)$$

where

$$\begin{aligned} F_1(x) &= -4x(1-x)(2Z_1 - K_1), \\ F_{m>1}(x) &= 4x(1-x) K_m, \end{aligned} \quad (16)$$

and K_m is the number of nearest-neighbor atoms shared by sites i and $i + m$. In an fcc lattice Z_m is 12, 6, 24, 12, 24, and 8 while K_m is 4, 4, 2, 1, 0 and 0 for shells $m = 1, 2, 3, 4, 5$, and 6, respectively. Note that $K_{m \geq 5} = 0$, hence $F_{m \geq 5} = 0$. From Eqs. (15) and (16) we have

$$\langle E_M \rangle_R = 4x(1-x) \frac{\lambda^2}{2} \left[-\frac{2Z_1^2}{R_1} + \sum_{m=1}^4 \frac{Z_m}{R_m} K_m \right]. \quad (17)$$

Equating this to the definition of Eq. (13) then gives the analytical result

$$\langle \alpha_M(x) \rangle_R = 4x(1-x) 0.7395182 \dots \quad (18)$$

We can also solve analytically for the effective interaction energies J_f , using the orthonormality of $\{\Pi_f(\sigma)\}$ [9] as follows [35]:

$$J_f = \frac{1}{2^N} \sum_{\sigma} \Pi_f(\sigma) E_M(\sigma) = \frac{1}{2^N} \sum_{\sigma} \Pi_f(\sigma) \frac{1}{2} \sum_{ij} \frac{Q_i(\sigma) Q_j(\sigma)}{|R_i - R_j|}. \quad (19)$$

Inserting our model of Eq. (12) yields

$$\begin{aligned} J_f &= \frac{\lambda^2}{2} \sum_{ij} \frac{1}{R_{ij}} \sum_{k,k'} \frac{1}{2^N} \sum_{\sigma} \Pi_f(\sigma) \left[S_i(\sigma) - S_k^{(i)}(\sigma) \right] \left[S_j(\sigma) - S_{k'}^{(j)}(\sigma) \right] \\ J_f &= \frac{\lambda^2}{2} \sum_{ij} \frac{1}{R_{ij}} \sum_{k,k'} \{ \delta_{f,ij} - \delta_{f,ik} \delta_{f,jk} + \delta_{f,kk'} \}, \end{aligned} \quad (20)$$

where $\delta_{f,ij}$ equals zero unless figure f equals the pair figure ij , etc. Equation (20) could be easily evaluated to give the analytic results for J_f , while Eq. (18) provides the analytic result for the Madelung constant of the random fcc alloy.

D. Solution via the Cluster Expansion

We next use the CE formalism to obtain the equivalent quantities. Using Ewald's method [36] we have calculated the "exact" Madelung constant $\alpha_M(\sigma)$ for $N_{\sigma} = 12$ fcc ordered structures depicted in Fig. 4, using the charge model of Eq. (12). (Figure 5 depicts, for comparison, the pseudobinary structures.) We then cluster-expand these $\{\alpha_M(\sigma)\}$ according to Eq. (3) using a set of N_F pair-interactions $\{J_m\}$ with $m = 1, 2, 3, 4$, and 5 [all many-body interaction energies vanish here, see Eq. (20)]. Minimizing the variance of Eq. (7) yields the interaction energies shown in Table I. We repeat the same procedure using $N_{\sigma} = 27$ structures. The Madelung constant of the random alloy, obtained with the cluster expansion is

$$\langle \alpha_M(R,x) \rangle_{CE} = 4x(1-x) 0.7368 \quad (\text{for } N_{\sigma} = 12) \quad (21a)$$

Table I. Comparison of exact and cluster-expanded (CE) results for the fcc Madelung lattice. Here, J_i gives the i th pair interaction energy (see text).

Interaction	J_0	J_1	J_2	J_3	J_4	J_5
Exact	0.7395	-0.3239	0.0825	0.0608	0.0345	0.0014
CE	0.7368	-0.3239	0.0835	0.0609	0.0348	0.0014

and

$$\langle \alpha_M(R,x) \rangle_{CE} = 4x(1-x)0.7392 \quad (\text{for } N_\sigma = 27) . \quad (21b)$$

This can be compared with the exact result of Eq. (18). Figure 3 shows a "ground state diagram" depicting the lowest-energy $T=0$ structures (searching 2^{16} configurations) of the Madelung lattice described by our CE, as well as the energy of the random fcc Madelung alloy. The S-CPA results for the random alloy are given for comparison.

E. Implications

There are a few obvious implications to this exercise.

(i) The cluster expansion converges reasonably rapidly even for the case of the (seemingly long-range) Madelung problem. This can be seen from the agreement between the exact model and the truncated CE for the $\langle \alpha_M \rangle_R$ values [Eqs. (18) vs (21)] and for the $\{J_F\}$ values (Table I).

(ii) The S-CPA based methods use $\langle E_M \rangle_R \equiv 0$, unlike the present result. While $\langle E_M \rangle_R \equiv 0$ is an exact *mathematical* result if uncorrelated charges $\langle Q_i Q_j \rangle = \langle Q_i \rangle \langle Q_j \rangle$ are assumed, this assumption is *physically* incorrect when charge transfer exists. Significant quantitative errors are expected for systems with non-negligible charge transfer (Fig. 3). These include possible errors in the electrostatic "ordering energies" $E_M(\sigma) - \langle E_M \rangle_R$, i.e., the difference in Madelung energy of an ordered structure σ and the random alloy of the same composition. In units of $(16\lambda)^2/2R$ these are [in parenthesis we give the S-CPA values]:

$$\begin{aligned} L1_0: & -0.8549 \quad (-1.5944) \\ L1_1: & +0.0444 \quad (-0.6951) \\ L1_2: & -0.6411 \quad (-1.1958) \\ DO_{22}: & -0.6623 \quad (-1.2169) . \end{aligned} \quad (22)$$

Having discussed the convergence of the CE in the simple case of the Madelung lattice, we now apply the method in the context of the local density approximation (LDA), where $E_{\text{direct}}(\sigma)$ of Eqs. (5)-(6) is calculated by the LDA. In this case, the electrostatic energy is calculated from the (continuous) electronic charge density, not from point charges.

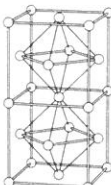
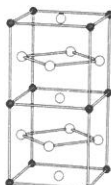
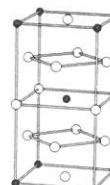

V. APPLICATION OF THE CE TO THE LATTICE-MATCHED AlAs/GaAs SEMICONDUCTOR ALLOY

We now illustrate the application of the CE method to the lattice-matched semiconductor alloy system $(\text{AlAs})_{1-x}(\text{GaAs})_x$, calculating the excess energies $\Delta E(\sigma, V)$ of Eq. (5) using the local density approximation, as implemented by the nonlocal pseudopotential plane-wave method. The procedure follows Sec. IV, namely:

(i) Define a set of N_G periodic crystals $A_p B_q$ representing a range of compositions and atomic plane orientations \hat{G} ; Table II and its caption give 27 examples (including the binaries) for the fcc symmetry. The structures are analogous to those depicted in Fig. 4 except that now we have an additional, fixed As sublattice that does not carry any statistical degrees of freedom. Figure 5 shows examples of the semiconductor structures used.

Table II. Calculated formation energies (in meV/4 atoms) of various ordered $A_p B_q$ structures ($A = \text{AlAs}$, $B = \text{GaAs}$). The structures can be characterized as superlattices of repeat periods (p, q) in various orientations given in this table, except for the luzonite AB_3 (predicted energy, 10.31; direct calculation, 10.42) and A_3B (predicted energy, 10.31; direct calculation, 10.16) which are not superlattices. Using the energies of six structures only (denoted by an asterisk) we predict via the cluster expansion the energies of the remaining 21 structures. In each case we list the predicted value and below it the value obtained directly from the *ab initio* calculation. The standard deviation for 21 predictions is 0.13 meV, close to the relative precision (~ 0.1 meV) of the underlying *ab initio* calculation.

Orientation formula	[111]	[001]	[110]	[201]	[113]
AB	CP	CA	CA	CA	CP
	10.74*	13.74*	13.74*	13.74*	10.74*
	10.74	13.74	13.74	13.74	10.74
AB_2	$\alpha 1$	$\beta 1$	$\gamma 1$	$\gamma 1$	$\gamma 1$
	7.39	9.57	11.39	11.39	11.39
	7.41	9.70	11.62	11.62	11.62
A_2B	$\alpha 2$	$\beta 2$	$\gamma 2$	$\gamma 2$	$\gamma 2$
	7.39	9.57	11.39	11.39	11.39
	7.50	9.88	11.66	11.66	11.66
AB_3	V1	Z1	Y1	F1	W1
	5.54	7.18	8.75	10.19	8.77
	5.49	7.12	8.68	10.31	8.78
A_2B_2	V2	Z2	Y2	CH	W2
	5.72	7.48*	10.64	13.50*	12.16
	5.65	7.48	10.48	13.50	12.13
A_3B	V3	Z3	Y3	F3	W3
	5.54	7.18	8.75	10.19	8.77
	5.55	7.22	8.65	10.13	8.74

SB Name: (other)	A1,(fcc)	L ₁₂	DO ₂₂	(β1, β2)
Formula:	A; B	A ₃ B ; AB ₃	A ₃ B ; AB ₃	A ₂ B ; AB ₂
Crystal Structure				
Example	Cu	Cu ₃ Au	TiAl ₃	
Bravais Lattice	Face-centered Cubic	Simple Cubic	Body-centered Tetragonal	Body-centered Tetragonal
Unit	(0, 1/2, 1/2)	(1, 0, 0)	(1, 0, 0)	(1/2, 1/2, 0)
Cell	(1/2, 0, 1/2)	(0, 1, 0)	(0, 1, 0)	(1/2, -1/2, 0)
Vectors	(1/2, 1/2, 0)	(0, 0, 1)	(1/2, 1/2, 1)	(1/2, 0, 3/2)
Space Group:				
Int. Tables:	Fm $\bar{3}$ m	Pm $\bar{3}$ m	I4/mmm	I4/mmm
Shoenflies:	O _h ⁵	O _h ¹	D _{4h} ¹⁷	D _{4h} ¹⁷
Number:	225	221	139	139
Pearson Symbol:	cF4	cP4	tI8	tI6
Equivalent Superlattice	None	None	A ₃ B along [201]	A ₂ B ₁ along [001]

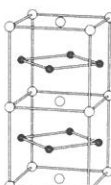
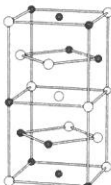
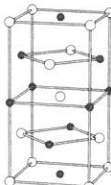
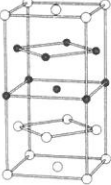
SB Name: (other)	L ₁₀	L ₁₁	(CH, "40")	(Z2)
Formula:	A B	A B	A ₂ B ₂	A ₂ B ₂
Crystal Structure				
Example	CuAu-I	CuPt	NbP	
Bravais Lattice	Simple Tetragonal	Rhombohedral (Triagonal)	Body-centered Tetragonal	Simple Tetragonal
Unit	(1/2, 1/2, 0)	(1/2, 1/2, 1)	(1, 0, 0)	(1/2, 1/2, 0)
Cell	(-1/2, 0, 1/2)	(1, 1/2, 1/2)	(0, 1, 0)	(-1/2, 1/2, 0)
Vectors	(0, 0, 1)	(1/2, 1, 1/2)	(1/2, 1/2, 1)	(0, 0, 2)
Space Group:				
Int. Tables:	P4/mmm	R $\bar{3}$ m	I4 ₁ /amd	P4/nmm
Shoenflies:	D _{4h} ¹	D _{3d} ⁵	D _{4h} ¹⁹	D _{4h} ⁷
Number:	123	166	141	129
Pearson Symbol:	tP4	hR32	tI8	tP8
Equivalent Superlattice	A ₁ B ₁ along [001]	A ₁ B ₁ along [111]	A ₂ B ₂ along [201]	A ₂ B ₂ along [001]

Figure 4. Crystal structure information for binary fcc compounds used in the cluster expansion.

(ii) Calculate quantum mechanically from band-structure theory the excess total energy $\Delta E_{\text{direct}}(\sigma)$ of these N_{σ} periodic structures. Here, the ion-ion, electron-ion, and electron-electron (Coulomb, exchange, and correlation) interactions are treated self-consistently in an *ab initio* fashion. Great care was exercised to assure that the calculated excess energies $\Delta E_{\text{direct}}(\sigma)$ have the same precision (within 0.1 meV/atom) for all structures; we use precisely equivalent basis sets, Brillouin-zone sampling, and stringent self-consistency conditions. These calculated energies $\Delta E(\sigma)_{\text{direct}}$ for all ordered structures σ exhibit a nonintuitive distribution whereby certain atomic-plane orientations [e.g., (111)] have the lowest energies, others [e.g., (201)] have the highest ones. This is illustrated in Figure 6.

(iii) Fit all of the $N_{\sigma} = 27$ calculated excess energies to a set of $N_F < N_{\sigma}$ interactions $\{J_{k,m}\}$. Here, k denotes the "order" of the interaction ($k=2,3,4$ are pairs, three and four body, respectively), and m denotes the separation ($m=1,2,3$, are first, second and third neighbors, respectively). Figure 1 depicts these figures. Using only $N_F = 13$ terms produces an excellent fit with the root-mean-square error of 0.097 meV, comparable to the intrinsic relative precision of the *ab initio* pseudopotential calculations. More importantly, these interactions $J_{k,m}$ show convergence with the size of the figure, e.g., the pair ($k = 2$) energies decay with interatomic separation m : they are -0.8075, -0.0279, -0.0225, -0.0051, -0.0001, and -0.0075 for $m = 1, 2, 3, 4, 5$, and 6, respectively. The same is true for the three-body terms $J_{3,1} = +0.0075$, $J_{3,2} = -0.0021$, and $J_{3,3} = +0.0003$, while the four-body terms are rather small: $J_{4,1} = +0.0009$ and $J_{4,2} = -0.0034$.

(iv) Given this rapid convergence, we now select a smaller number of figures, i.e., those that give the largest contribution $D_{k,m}J_{k,m}$ to the energy of Eq. (3) and use these J 's to *predict* the energies of other structures (not used as input), *viz* Eqs. (3b)-(3c). In addition to the normalization terms $(k,m) = (0,1)$ and $(1,1)$, we use the pair interactions (2,1), (2,2), (2,3), and (2,4). Using just these $N_F = 6$ figures and $N_{\sigma} = 6$ structures (denoted in Table II by asterisks)

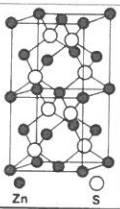
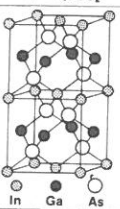
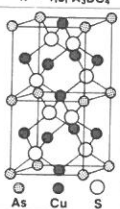
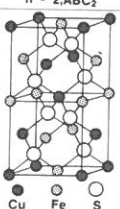
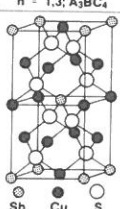
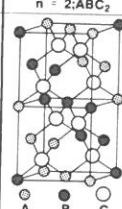
Ordering Vectors	(0,0,0)	(0,0,1)		(2,0,1)		(1,1,1)
Name (ternary)	Zincblende (Sphalerite)	Layered Tetragonal	"Luzonite"	Chalcopyrite	Famatinite	Layered Trigonal
Formula	$n = 0.4; AC$	$n = 2; ABC_2$	$n = 1.3; A_3BC_4$	$n = 2; ABC_2$	$n = 1.3; A_3BC_4$	$n = 2; ABC_2$
						
Example (ternary)	ZnS type	InGaAs ₂ type	Cu ₃ AsS ₄ type	CuFeS ₂ type	Cu ₃ SbS ₄ type	CrCuS ₂ type (NaVS ₂)

Figure 5. Crystal structures information for pseudobinary fcc compounds.

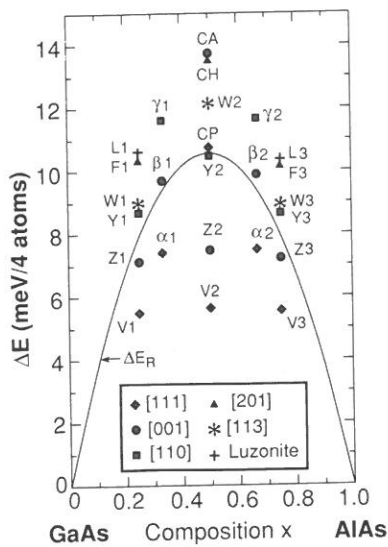


Figure 6. *Ab initio* calculated formation energies of the various $Al_pGa_qAs_{p+q}$ ordered structures of Table II. Solid line gives the calculated energy of the random $Al_{1-x}Ga_xAs$ alloy. The symbols refer to the structures defined in Table II. From ref [13].

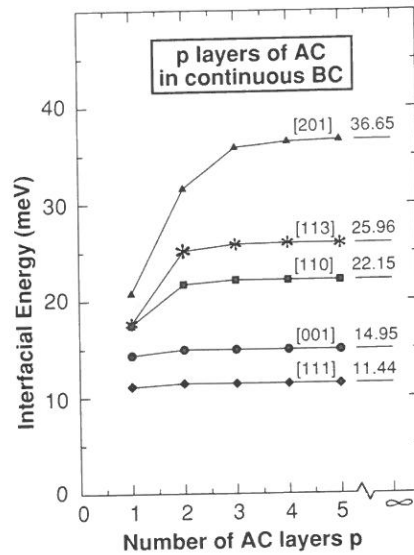


Figure 7. Predicted interfacial energies of quantum wells consisting of p layers of AC embedded in a continuous BC barrier. Note that insertion in the [111] direction has the lowest energy. From ref [13].

we obtain by direct matrix inversion [Eq. (8)] a set of six interaction energies. These are now used to *predict* the energies of the *remaining* 21 structures, whose energies were not used in the determination of the J_F 's. Table II shows that direct calculations on only 6 structures can be used to predict the quantum mechanically calculated excess energies with useful precision: the prediction error (0.13 meV; a similar value is obtained by selecting other structures) is just slightly larger than the intrinsic precision of the *direct* pseudopotential calculation. *This analysis shows that the informational content of the complex total-energy calculations on various $(AlAs)_p(GaAs)_q$ structures can be reduced to ~ 6 interaction energies and that these suffice to predict the structural energies of other configurations.*

There are a number of obvious applications to this cluster-expansion:

(i) **Calculation of mixing enthalpy:** We can predict the mixing enthalpy of a *random* $A_{1-x}B_x$ alloy [Eq. (4)] by replacing $\bar{\Pi}_{k,m}(\sigma)$ in Eq. (4) by its configurationally averaged value $(2x - 1)^k$. Using the interaction energies $\{J_{k,m}\}$ from the $N_\sigma = N_F = 6$ set we get the excess energy of the random alloy depicted in Fig. 6 by the solid line. The value at $x = 1/2$ is within the experimentally determined range [37].

(ii) **Ground state search:** A ground-state search with the Ising Hamiltonian (3) using our interaction energies $\{J_{k,m}\}$ shows that the system will phase separate into AlAs + GaAs at $T = 0$. This is consistent with the behavior of this systems [37].

(iii) **Prediction of superlattice energies:** Given the interaction energies, it is possible to predict from Eq. (3) the formation enthalpies of $(\text{AlAs})_p(\text{GaAs})_q$ *superlattices* as a function of the repeat periods (p,q) and layer orientation \hat{G} simply by calculating the geometrical correlation functions $\bar{\Pi}_F(p,q,\hat{G})$ and using the interaction energies that were determined previously from our fit (Table II). For equimolar repeat periods (p,p) we predict [8c,13] the order of the formation enthalpies $\Delta E(111) < \Delta E(001) < \Delta E(110) < \Delta E(113) < \Delta E(201)$. In the few cases where our ΔE can be compared with direct *ab initio* superlattice calculations (for structures not included in our basis set), the agreement is good, e.g., for the $p=q=3$ and $\hat{G} = (111)$ oriented superlattice the result obtained from our cluster expansion, 11.4 meV/cell, is in very good agreement with the extensive first-principles calculations [13] yielding 11.6 meV/cell.

(iv) **Prediction of interfacial energies:** The cluster expansion can be used to extract the interfacial energy for the interesting case of $(\text{BC})_\infty(\text{AC})_p(\text{BC})_\infty$ *quantum wells*, i.e., p layers of AC embedded in a continuous barrier made of BC. The results [13] are shown in Fig. 7. We predict that a [111]-oriented well is the most stable while the [201] is the least stable in this series. The different behaviors versus p and, for fixed p, versus orientation \hat{G} can be understood in terms of the number of mixed A-B atom pairs at the interface for each geometry [13]. Application of the CE to the calculation of anti-phase-boundaries in GaAlAs_2 is further described in Ref. [13].

To summarize, we have shown that in the case of lattice-matched semiconductor alloys one obtains a rapidly-convergent cluster expansion that permits ground state searches as well as predicting energies of "complex structures", not currently amenable to direct first-principles calculations. We next give a brief overview on the overall trends obtained for other semiconductor alloys, i.e., those exhibiting size-*mismatched* constituents.

VI. APPLICATION TO SEMICONDUCTOR PHASE DIAGRAMS

The cluster expansion method can also be applied to lattice-mismatched semiconductors (although it leads to slower convergence discussed in Sec. IX below). The main results we find [8] are:

(i) Lattice-mismatched semiconductor alloys have positive formation and mixing enthalpies $\Delta H = \Delta E_{\text{VD}} + \Delta E_{\text{chem}} > 0$ because the positive elastic "volume deformation" energies ΔE_{VD} exceed in magnitude the negative "chemical energies" ΔE_{chem} (this is discussed in more detail in Sec. VI.D). Because the total $\Delta H > 0$, the ground state corresponds to phase-separation. The CVM-calculated phase-diagrams (Fig. 8) hence show miscibility gaps. The calculated shape of the miscibility line agrees with the experiment in the one case where detailed data is available ($\text{GaSb}_{1-x}\text{As}_x$, see Fig. 8e). The maximum miscibility temperature scales with the relative size

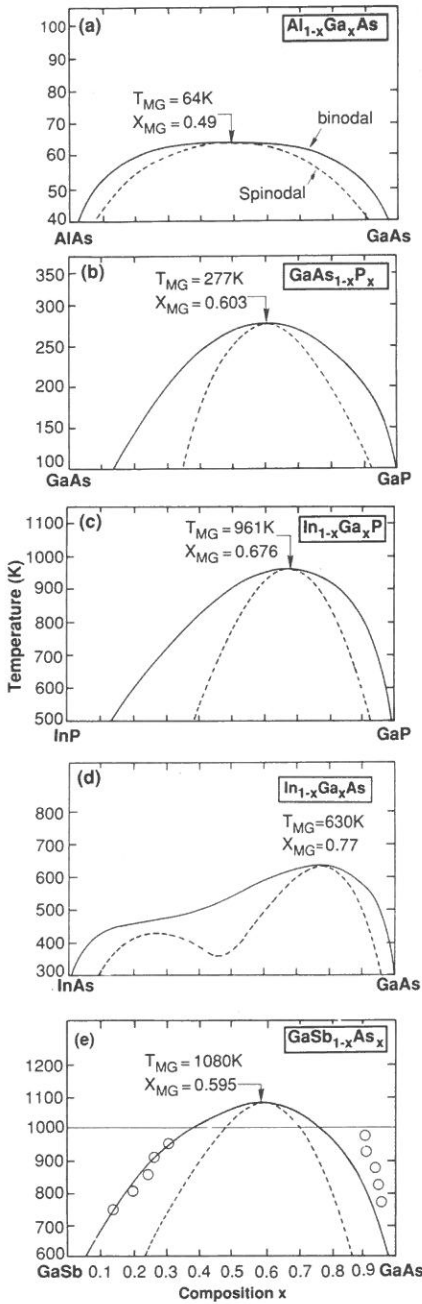


Figure 8. Calculated phase diagrams for the III-V alloys. The solid (dashed) lines give the binodal (spinodal) lines. Low-temperature ordered phases are not shown. The arrows point to the maximum miscibility gap (MG) temperatures and compositions. The circles in part (e) are the recent experimental data of Ishide et al. *J. Less. Comm. Metals* **142**, 135 (1988); the horizontal line represents the peritectic line. From ref [8].

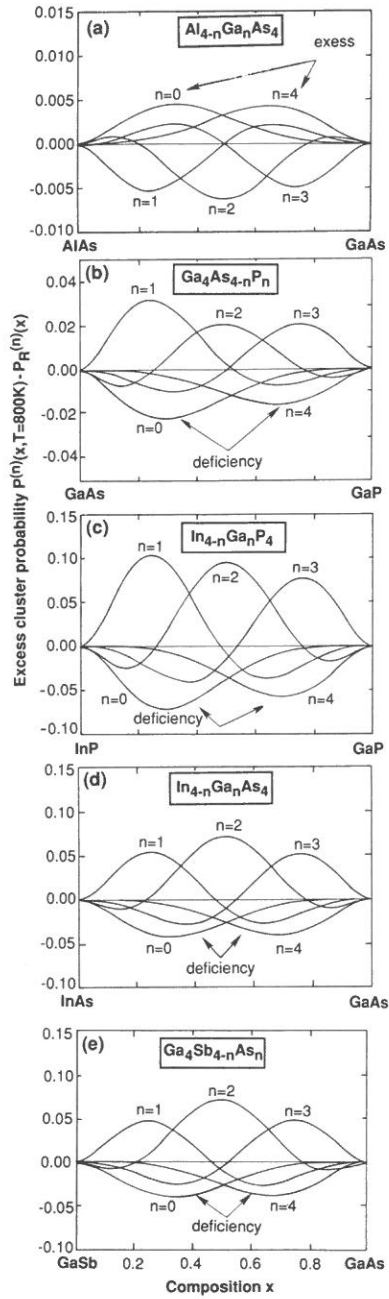


Figure 9. Excess cluster probabilities $\Delta P_n(x, T)$ at $T = 800$ K, with respect to the values obtained for a perfectly random alloy [Eq. (23)]. Observe the (small) clustering in the size-matched $\text{Al}_{1-x}\text{Ga}_x\text{As}$ system and the (larger) anticlustering found in the size-mismatched systems (all others). Results are given for the III-V systems whose clusters are denoted (a) $\text{Al}_{4-n}\text{Ga}_n\text{As}_4$, (b) $\text{Ga}_4\text{As}_{4-n}\text{P}_n$, (c) $\text{In}_{4-n}\text{Ga}_n\text{P}_4$, (d) $\text{In}_{4-n}\text{Ga}_n\text{As}_4$ and (e) $\text{Ga}_4\text{Sb}_{4-n}\text{As}_n$. From ref [8].

mismatch $la_A - a_B/a$. Despite this, the random alloy exhibits ordering type short range order (Fig. 9 below). The reason is as follows:

(ii) The main contribution to these chemical energies comes from atomic relaxations at fixed volumes. Relaxation is illustrated in Fig. 10: it shows the calculated nearest-neighbor bond lengths in a number of III-V alloys. They are seen to deviate dramatically from what an unrelaxed, static lattice model (underlying the S-CPA and VCA) would assume. That the non-elastic, "chemical" energies ΔE_{chem} are antiferromagnetic can be seen from the predicted short range order. Figure 9 shows the calculated "excess probability"

$$\Delta P_n(x,T) = P_n(x,T) - P_n^{\text{random}}(x) \quad (23)$$

for finding at (x,T) a $A_{4-n}B_n$ cluster, in excess of what the random (Bernoulli) probability will grant. We see that for all lattice mismatched alloys one predicts that the *mixed* clusters A_3B , A_2B_2 , and AB_3 have a *higher* probability than in random statistics i.e., the system shows "anticlustering"-type short range order (SRO). Hence, despite the fact that the ground state is phase separating ($\Delta E_{\text{VD}} + \Delta E_{\text{chem}} > 0$) the disordered phase shows short range order ($\Delta E_{\text{chem}} < 0$). In the lattice-*matched* case of AlAs/GaAs one has $\Delta E_{\text{VD}} = 0$ and $\Delta E_{\text{chem}} > 0$, so the SRO is in the form of clustering (Fig. 9a).

(iii) Different ordered structures have different abilities to accommodate dissimilar bond lengths. The chalcopyrite structure CH is, in fact, best able to pack different A-C and B-C bonds (even relative to the random alloy), hence its ΔE_{chem} is the most negative of all structures. Consequently, unlike the case in lattice-matched systems (Fig. 11a), in lattice mismatched systems (Fig. 11b) the CH structure has a lower $T = 0$ energy than the random alloy. In other words, the ordering energy $E(\sigma) - \langle E \rangle_R$ is negative for CH.

(iv) Since the chalcopyrite structure is stabler at $T = 0$ than the random alloy, one expects to find this structure as a *metastable* bulk ordered phase below some temperature T_c . This phase will be observed if *local* atomic diffusion is allowed, but long-range atomic rearrangements (which would have led to phase-separation) are kinetically too slow at low temperatures. The transition temperatures T_c for this metastable order-disorder transformation was predicted [8a,b] for many III-V and II-VI alloys and found to be rather low ($T \leq 600$ K). Experimental testing of this result would be desirable.

(v) One could conceive of a way of making the *metastable* bulk ordered structure (resulting from attractive chemical interactions) *stable*: Since the ordered chalcopyrite structure is lower in energy at $T = 0$ than the random alloy but is higher in energy than equilibrium phase-separation (Fig. 11b), removal of phase-separation from contention could expose the ordered structure as the absolutely lowest energy phase (Fig. 11c). This could be done by *epitaxy*: grow the $A_{1-x}B_x$ alloy or the ordered AB compound coherently on a substrate that is lattice matched to it, but is mismatched with pure A and pure B. This would destabilize the coherent epitaxial

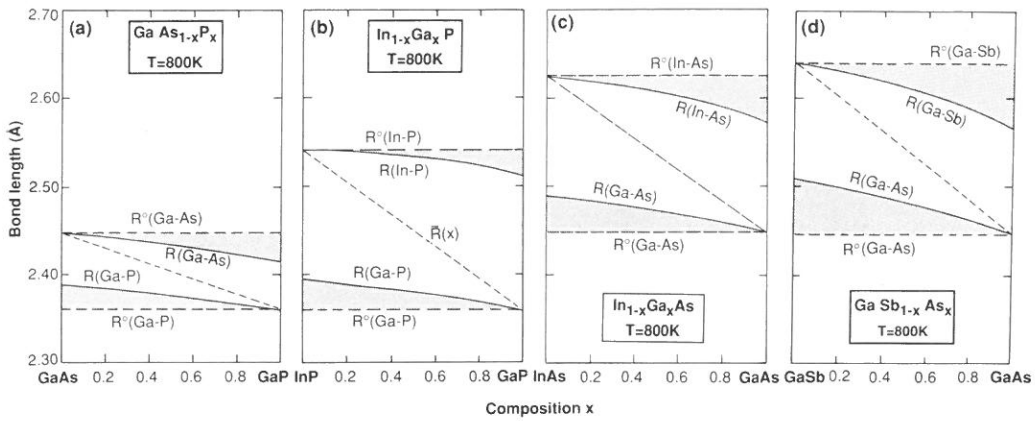


Figure 10. Calculated equilibrium alloy bond lengths $R(A-C)$ and $R(B-C)$ at $T=800$ K (solid lines) for size-mismatched systems, compared with the "ideal" zinc-blende values $R^0(A-C)$ and $R^0(B-C)$ (dashed horizontal lines). The VCA value $R(x)$ is given for comparison. The shaded areas represent deviations of equilibrium alloy bond lengths from the "ideal" values. From ref [8b].

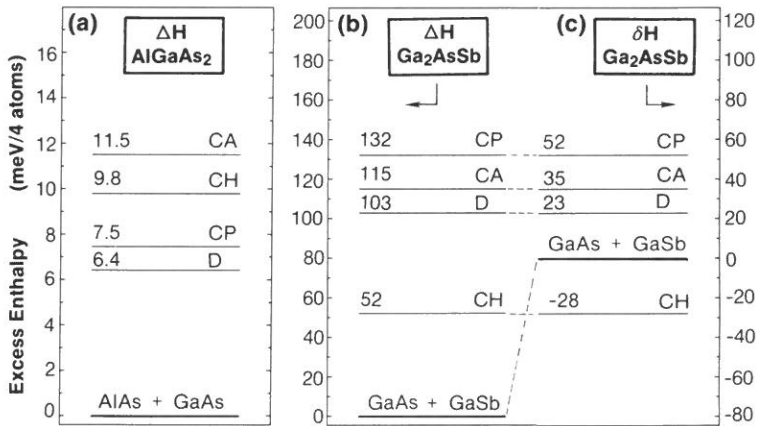


Figure 11. Calculated excess enthalpies of the lattice-matched $AlGaAs_2$ (part a) and the lattice-mismatched Ga_2AsSb system (parts b and c). Part (c) gives the *epitaxial* energies where $GaAs + GaSb$ are coherently confined to a substrate whose (001) lattice constant equals that of $GaAs_{0.5}Sb_{0.5}$. CA = $L1_0$; CH = "40"; CP = $L1_1$, and D = disordered. From ref [8a]. Note that epitaxy converts the CH structure from metastable (Part b) to stable (Part c).

constituents (A-on-AB and B-on-AB) relative to the epitaxial alloy (Fig. 11c). Figure 12 shows [38] how an *epitaxial* phase diagram exhibits stability of the bulk-metastable chalcopyrite compound, and also lowers dramatically the miscibility temperature of the alloy. This illustrates how epitaxy could lead to stabilization of bulk-unstable ordered compounds, and to reduction of the immiscibility temperature.

Many of our predictions for the structural and thermodynamic properties of lattice-mismatched semiconductor alloys await experimental testing. These include (i) more measurements of *bulk* phase diagrams (Fig. 8), (ii) observation of *metastable* chalcopyrite

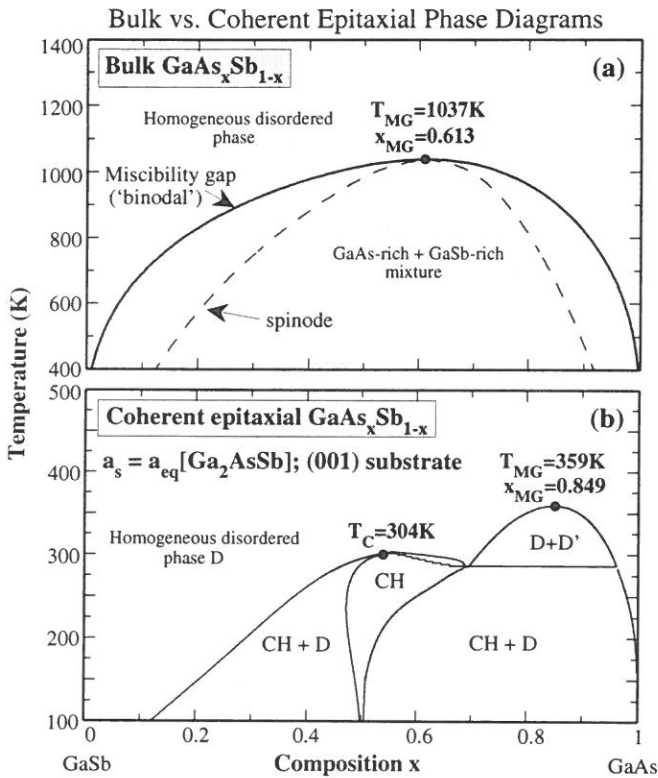


Figure 12. Calculated (x,T) phase diagrams for $GaAs_xSb_{1-x}$ under bulk [panel (a)] and coherent epitaxial conditions on an (001) substrate lattice-matched to $x = 1/2$ [panel (b)]. D and D' indicate disordered phases of distinct compositions. 'Spinode' in (a) indicates limits of metastability of homogeneous disordered phase. Note how epitaxy converts the bulk immiscibility into ordering. From ref [38].

ordering in low-temperature *bulk* samples, (iii) observation of SRO of the form suggested in Fig. 9, and (iv) observation of *stable* chalcopyrite ordering in coherent *epitaxial* samples (Fig. 12). Since more experimental data are available on transition metal alloys, we next describe the application of the cluster expansion to such systems.

VII. APPLICATION TO BINARY PLATINUM ALLOYS

A. The Issue

One of the well-known metallurgical rules is that binary transition metal systems whose constituent atoms have nearly-filled d shells ("late transition metals") have *positive* mixing enthalpies ΔH_f and show, at low temperatures, phase-separation rather than long-range ordering. This has been explained in terms of tight-binding d band filling arguments [39-41]: it was found that even in the absence of size-mismatch between the constituents [40] occupation of the upper

"antibonding" part of the d band leads universally to $\Delta H_f > 0$ for all late TM's with an average d electron count $\bar{N} \geq 8$.

The actual situation appears to be more complex as illustrated for example, by the phase-behavior of binary alloys of Pt with its neighboring elements in the Periodic Table [42,43]. First, even discarding for a moment "special cases" such as the ordering Pt-Cu and Pt-Ag intermetallics [42], that contain a noble metal, or the ordering [42,43] Pt-Co system which is complicated by a magnetic behavior over a wide composition range, the fact that even the non-magnetic Pt_{0.5}Ni_{0.5} alloy orders defies all current d band theories [39]-[41]. While it is certainly possible to fit the observed Pt-Ni phase diagram to an Ising model [44], attempts to explain even the *sign* of the Ising interaction energies required to produce the fit, have all failed [41]. Second, while Pt-Rh and Pt-Pd were surmised [2,42] to phase separate, examination of the original data [45] shows that no evidence exists to this effect (they were measured only at very high temperatures where solid solutions exist [42]). Only a suggestive extrapolation from the known behavior of Pd-Rh and Pd-Ir exists. In fact, measurements on Pt-Pd have shown *negative* mixing enthalpies [46] and clear evidence in X-ray diffuse scattering [47] for a substantial degree of short-range order which remains unexplained.

B. The Effective Interaction Energies and Ground States

We have applied the CE to this problem by calculating $\Delta E(V, \sigma)$ of Eq. (5) using the scalar-relativistic LAPW method [48] for 12 simple ordered structures shown in Fig. 4. To test the transferability of $\{J_F\}$ we have recalculated these from a *subset* of $N_\sigma = 10$ (out of a total of 12) of our ordered structures, then used these new J 's to predict through Eq. (3) the formation enthalpies of the *remaining* two structures, not included in the fit. Testing a number of different choices of 10 out of 12 structures gives an average "prediction error" (relative to direct LAPW calculations) that is comparable to the underlying error of LAPW itself. We can hence use these sets of $\{J_F\}$ to predict through Eq. (3) the energies of *arbitrary* fcc lattice configurations that are too numerous and often too complex to directly calculate by the LDA.

The effective interactions resulting from the full fits are depicted in Fig. 13. They show: (i) a reasonably rapid decay with interatomic distance, (ii) a non-monotonic order of energies, e.g., $J_{2,3} > J_{2,2}$ in Pt-Cu, (iii) that the dominant interactions in Pd-Rh are "ferromagnetic" ($J < 0$ i.e., repulsive), indicating phase-separation, but "antiferromagnetic" (attractive) in Pt-Cu, Pt-Pd, and Pt-Rh, implying [10] different types of ordering vectors.

We have used these effective interaction energies to perform a ground state search [8a] comparing different structures at the same composition as well as the stability of the homogeneous structure against mixing of two (ordered or disordered) phases of different

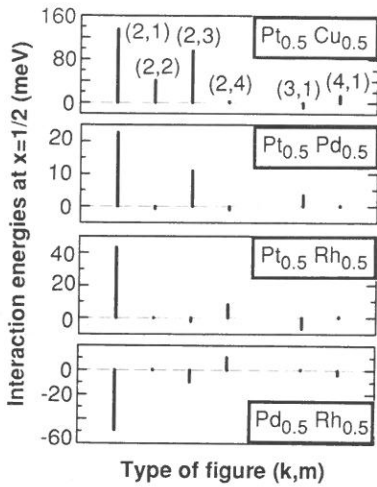


Figure 13. Calculated k -body m th-neighbor cluster interaction energies $J_{k,m}$ at $x = 1/2$, for Pt-based binary alloys. From ref [29].

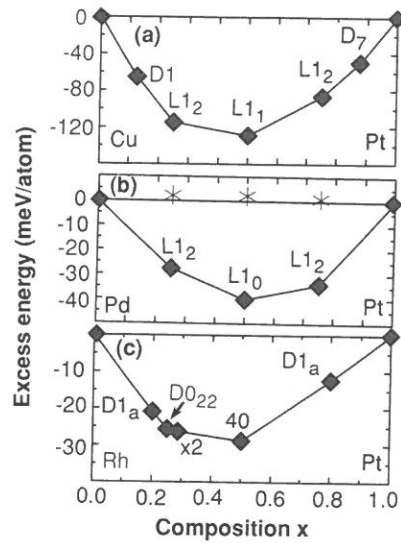


Figure 14. Predicted $T = 0$ ground states (diamond-like symbols) of Pt-based binaries as a function of composition. $D1_a$ is the $MoNi_4$ -type A_4B superlattice along $[201]$, "X2" is the A_5B_2 superlattice along $[201]$, and $D1$ (AB_7) and $D7$ (AB_7) are fcc-like structures with the unit cell vectors double that of the underlying fcc unit vectors. Crosses in part (b) show non-relativistic results that indicate that in the absence of relativistic effects the ground state of Pt-Pd is phase separating. From ref [29].

compositions. The resulting ground state lines are shown in Fig. 14. These show that (i) Pd-Rh phase separates, as found experimentally [45,49] and by other calculations [50], but (ii) Pt-Cu, Pt-Pd, and Pt-Rh are found to order in $[1/2, 1/2, 1/2]$, $[001]$, and $[10\bar{1}2]$ ordering vectors, respectively, in conflict with expectations based on tight-binding model [2,39]. If, however, one uses a non-relativistic calculation of $E_{direct}(\sigma)$, the predicted ground state of Pd-Pt is phase separation (denoted by asterisks in Fig. 14b). For $Pt_{0.5}Cu_{0.5}$ we correctly find trigonal $L1_1$ ordering showing that our expansion captures the delicate competition between trigonal ($L1_1$) and tetragonal ($L1_0$) structures (we find, however, that $L1_0$ is stabler than $L1_1$ if one assumes the nearest-neighbor approximation of Ref. 7). No low temperature data exist for Pt-Rh. For $Pt_{0.51}Pd_{0.49}$, X-ray diffuse scattering experiments [47] revealed significant short range order in the nominally disordered alloy; while the crystal structure (or phase diagram) was not determined, the average number of Pt first-neighbors to Pd is consistent with tendencies to order in the structure predicted here. It is interesting to note that our ground-state search also identifies new structures that were *not used* to determine the interaction energies, e.g., $D1$ and $D7$ for Cu-Pt, and $D1_a$ and $X2$ for Rh-Pt [29]. Hence, the cluster expansion method permits detection of *unsuspected* ordered structures.

C. Thermodynamic Properties

Using the set of interaction energies $\{J_{k,m}\}$ we have solved the spin- $\frac{1}{2}$ fcc generalized Ising model in the cluster-variation method [11] (CVM), evaluating the configurational entropy by folding interactions within figures that are larger than the tetrahedron (this method agrees closely with Monte Carlo simulations; see Fig. 15 in Ref. 8b). Of the systems studied here in detail, we display finite-temperature results only in the cases where experimental data are available for comparison. Figure 15(a) compares for Pd-Rh the calculated phase diagram with experiment [49]. The agreement is reasonable, given that no empirical data or parameter adjustment is used and that vibrational and coherency effects are neglected. This figure also shows that the calculated phase diagram can be brought into *perfect* agreement with experiment if our reduced excess enthalpy ΔH is lowered by a reasonable error margin of 12%. Figure 15(b) depicts for Pt-Pd the calculated mixing enthalpy and the excess free energy, showing good agreement with experimental data [46]. The Ni-Al phase diagram (Fig. 16) will be discussed later.

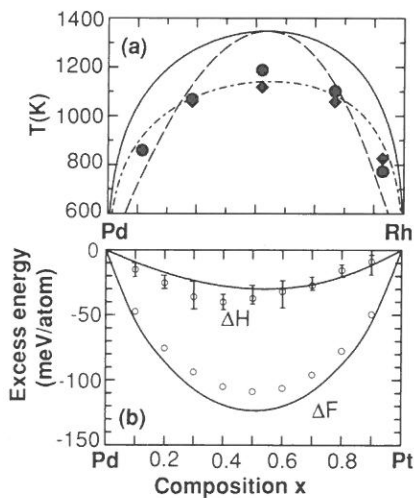


Figure 15. (a) Calculated (lines) and measured (circles from Ref. 49a and diamonds from Ref. 49b) phase diagram of Pd_{1-x}Rh_x. The solid line is the binodal, the dashed line is the spinodal, and the dash-dot line is the calculated binodal corresponding to a ~12% reduction in ΔH . (b) Calculated and measured (Ref. 46) excess enthalpy ΔH (at $T=300$ K) and free energy ΔF (at $T=1600$ K) for Pt_xPd_{1-x}. From Ref. [29].

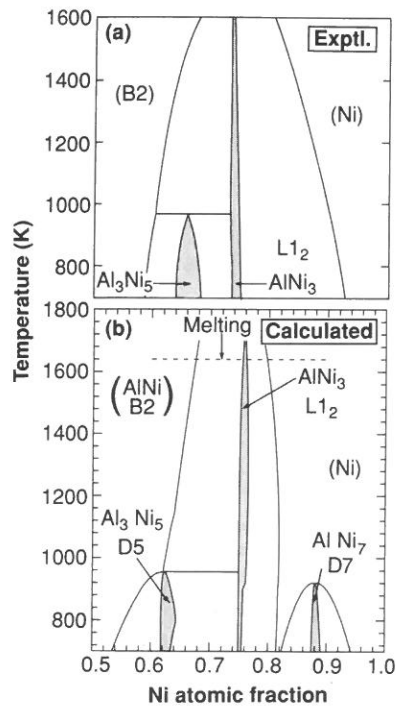


Figure 16. (a) Experimental (Ref. 42,54) and (b) CVM calculations for the phase diagram of Al_{1-x}Ni_x for $x \geq 0.5$. Vibrational entropy and liquid-state effects were neglected. From Ref [28].

We next present the methodology used to analyze the electronic origins of ordering and phase-separation in these systems [51].

D. Method of Analysis

The large body of phase-diagrams collected over the years has been used in the past to deduce many important phenomenological rules of phase stability. These have had enormous value in systematizing the large data bases in terms of elementary constructs such as the "size factor," "electron per atom ratio," the "electrochemical factor," and "Brillouin zone effects." It is essential that modern quantum mechanical calculations not only produce "correct results," but also help demystify the classical metallurgical rules in terms of recognizable and quantifiable concepts. I illustrate here how the CE method can be used to analyze its own predictions.

To analyze the underlying physics of the results of the preceding section recall that the central energetic quantities used in theoretical discussions of phase stability are the formation enthalpy $\Delta H_f(\sigma_x)$ of the ordered (ord) compound A/B in structure σ and the mixing enthalpy $\Delta H_{\text{mix}}(x)$ of a random (rand) alloy $A_{1-x}B_x$ of composition x . These are defined as the excess energies taken with respect to the equivalent amounts of the solid constituents A and B at their equilibrium volumes V_A and V_B :

$$\Delta H_f(\sigma_x) = E_\sigma(\text{ord}) - [(1-x)E_A + xE_B] \quad (24)$$

$$\Delta H_{\text{mix}}(x) = E_\sigma(\text{rand}) - [(1-x)E_A + xE_B] . \quad (25)$$

The "ordering energy" is defined as the difference

$$\delta E_{\text{ord}}(\sigma_x) = \Delta H_f(\sigma_x) - \Delta H_{\text{mix}}(x) . \quad (26)$$

If $\delta E_{\text{ord}} < 0$, the random alloy could develop short range order of the type underlying the structure σ . When $\Delta H_f(\sigma) < 0$, the long range ordered configuration σ could become a stable "ground state structure", whereas $\Delta H_f(\sigma) > 0$ means that the ordered structure σ is unstable with respect to phase-separation into A and B.

Further insight into the factors governing such stability trends can be obtained by decomposing the energies (24)-(25) into a sequential process [24] as follows:

First, deform hydrostatically pure A and B from their equilibrium volumes V_A and V_B to the volume V_σ akin to the final compound σ with the composition x . In doing so we invest a "volume deformation" (VD) energy ΔE_{VD} : it vanishes if the constituents are size-matched ($V_A = V_B \equiv V_\sigma$) and is *positive* (i.e., promotes phase-separation) otherwise. Since, to within a good approximation, the molar volumes of structures at the same composition are equal [17], ΔE_{VD} depends essentially on the composition x but not on the atomic configuration σ .

Second, permit $A(V_\sigma)$ and $B(V_\sigma)$, both prepared at the final volume V_σ to form the compound $\sigma(V_\sigma)$ in its ideal structure. In this constant-volume and constant-geometry reaction

one permits charge-transfer, the formation of hybridized energy bands, etc.; the energy change will thus be called the "charge transfer" (CT) energy ΔE_{CT} .

Finally, permit the atoms in configuration σ to relax to their energy-minimizing positions. Such strain-relieving relaxations (REL) change the energy by $\Delta E_{REL}(\sigma)$. This includes both cell-internal displacements as well as cell-external deformation (e.g., changing the c/a ratio in the $L1_0$ structure). Like the volume deformation, the energy, $\Delta E_{REL}(\sigma)$ too tends to vanish for size-matched systems. In contrast to ΔE_{VD} , however, relaxations depend on the atomic configuration σ and are energy lowering (i.e., promote ordering).

We will compute the above mentioned components of ΔH

$$\Delta H_f(\sigma) = \Delta E_{VD}(x) + \Delta E_{CT}(\sigma) + \Delta E_{REL}(\sigma) \quad (27)$$

directly from their definitions as differences in the appropriate total energies, thus quantitatively isolating various factors governing phase-stability. We will further repeat the calculations using a constrained Hamiltonian (i.e., relativistic vs non-relativistic) finding how certain electronic interactions affect phase-stability [see Eq. (3d)]. The energy of the random alloy is calculated from Eq. (4). Since the input to Eq. (7) is a set $\{\Delta H_f(\sigma)\}$ of formation enthalpies for ordered compounds, and since each of these can be decomposed accordingly to Eq. (27), the final random alloy energy $\Delta H_{mix}(x)$ can also be represented in the form (27). Consequently, the "ordering energy" of Eq. (26) can be expressed as

$$\delta E_{ord}(\sigma) = [\Delta E_{CT}(ord) - \Delta E_{CT}(rand)] + [\Delta E_{REL}(ord) - \Delta E_{REL}(rand)] , \quad (28)$$

permitting its analysis in terms of *excess* relaxation and charge-exchange relative to the random alloy. The first term of Eq. (28) represents qualitatively the classic "electronegativity factor," while the second term represents the "size factor."

E. Relatively-Induced Ordering (NiPt) and Phase-Separation (AuPt)

The method of analysis of the previous section are illustrated in Table III for Au-Pt, Ni-Pt, and Ni-Au, respectively [51]. Our analysis shows the following features:

(i) A *non-relativistic* description of NiPt predicts $\Delta H_f > 0$, i.e., phase-separation, despite the fact that the ordering energy $\delta E_{ord}(L1_0)$ is negative. Neglecting ΔE_{VD} and ΔE_{REL} , Pinski et al. [52] have previously calculated (non-relativistically) the finite-temperature generalization of δE_{ord} and from it the long range order (LRO). They predicted an ordering transition into the $L1_0$ structure at the temperature of $T_c \sim 1500$ K. However, since the non-relativistic description used by them gives $\Delta H_f(L1_0) > 0$ (Table III), the system must phase-separate rather than order. Hence, a correct non-relativistic description does not produce LRO at *any* temperature. This illustrates the fact that neglect of relaxation can lead to large errors (~ 1500 K) in order-disorder transition temperatures, and that in general, LRO cannot be predicted from a theory of δE_{ord} . A similar conclusion is apparent in the relativistic description of NiAu (Table III): we find that

Table III. Contributions of volume deformation (VD), charge-exchange (CT), and relaxation (REL) to the excess enthalpies [Eqs. (27) and (28)]. Results are in meV/atom.

	Non-Relativistic		Relativistic	
	$L1_0$	Random	$L1_0$	Random
	$Ni_{0.5}Pt_{0.5}$			
ΔE_{VD}	+543.6	+543.6	+426.8	+426.8
ΔE_{CT}	-398.4	-307.0	-504.5	-403.3
ΔE_{REL}	-51.6	-60.5	-18.0	-53.8
ΔH	+93.6	+176.1	-95.7	-30.3
δE_{ord}	-82.5		-65.4	
	$Au_{0.5}Pt_{0.5}$			
ΔE_{VD}	+42.3	+42.3	+48.6	+48.6
ΔE_{CT}	-113.5	-103.5	+28.2	+1.5
ΔE_{REL}	~0	~0	~0	~0
ΔH	-71.2	-61.2	+76.8	+50.1
δE_{ord}	-10.0		+26.7	
	$Ni_{0.5}Au_{0.5}$			
ΔE_{VD}	+722.2	+722.2	+561.8	+561.8
ΔE_{CT}	-337.8	-283.8	-464.8	-369.2
ΔE_{REL}	-11.9	-82.5	-20.2	-68.3
ΔH	+372.5	+355.9	+76.8	+124.3
δE_{ord}	+16.6		-47.5	

$\Delta H_f(L1_0) > 0$ despite $\delta E_{ord}(L1_0) < 0$. This is consistent with the observation of (001) short range order in high temperature NiAu alloys which phase separates at lower temperatures [53].

(ii) The reason that the non-relativistic ground state of NiPt is phase-separation is the dominance of volume deformation over charge-exchange and relaxation (Table III). Indeed, the calculated non-relativistic lattice constants of the fcc constituents shows a large (16.6%) relative size mismatch leading to a large destabilizing ΔE_{VD} . Relativity stabilizes NiPt for two reasons. First, it reduces the size mismatch to 12.9%. The relativistic reduction in size mismatch leads to a reduction in ΔE_{VD} , hence, stabilization. The same effect exists in other compounds in which only *one* of the two elements is heavy; see for example ΔE_{VD} in NiAu, Table III. Second, relativity leads to a significant lowering of ΔE_{CT} . Examination of the density of states and charge transfer shows the reason: relativistic effects lower the Pt s band more than the Ni s band, leading to a more effective Ni→Pt charge transfer and s-d hybridization. The combined

effect of reduced repulsiveness of ΔE_{VD} and increased attractiveness of ΔE_{CT} leads in a relativistic description to a negative $\Delta H_f(L1_0) = -95.7$ meV/atom, i.e., ordering.

(iii) A *non-relativistic* description of AuPt leads to ordering, while a relativistic description leads to the observed phase-separating behavior: The reason is again two-folded. First, while relativity does not significantly change the lattice mismatch if both atoms are heavy, it raises significantly the bulk moduli B of heavy elements: non-relativistically $B_{Pt} = 1.79$ Mbar and $B_{Au} = 1.03$ Mbar, while relativistically $B_{Pt} = 2.87$ Mbar and $B_{Au} = 1.83$ Mbar. (The measured values are 2.78 Mbar and 1.73 Mbar, respectively.) This leads to a (small) relativistic *increase* in ΔE_{VD} hence, destabilization. Second, relativity *diminishes* strongly the stabilizing effects of charge-exchange in AuPt (indeed, it even changes the sign of ΔE_{CT} ; see Table III). The reason is evident by inspecting the calculated electronic structure of fcc Au, Pt, and $L1_0$ AuPt (all evaluated at the same $L1_0$ atomic volume): Au has 11 valence electrons and exhibits s-like states at the Fermi surface, while Pt has only 10 valence electrons and exhibits d states at the Fermi surface. In a non-relativistic description there is a significant stabilizing charge-transfer from the higher Au s-p band into the Pt d band. However, relativity shifts the Au s band to deeper binding energies; this band is then less able to provide charge to the Pt d band (the Pt charge now comes predominantly from the Au d band). Hence, ordered AuPt is less stable in a relativistic description. Simple d band models miss these effects.

Considering the Au-Ni-Pt triangle, we conclude that when *both* elements are heavy (AuPt), relativity promotes phase-separation through *increased* ΔE_{VD} and *diminished* ΔE_{CT} , while when

only one of the two elements is heavy (NiPt and NiAu), relativity *reduces* ΔE_{VD} and *increases* ΔE_{CT} , thus contributing to ordering.

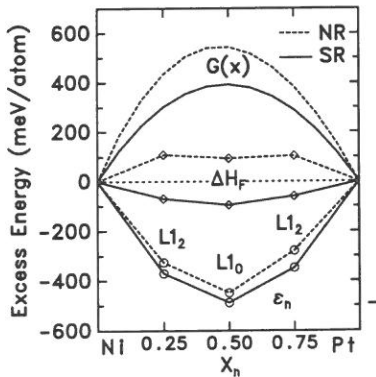


Figure 17. ϵ - G decomposition (Ref [17]) of the excess energies of Ni-Pt using a non-relativistic (NR) and scalar relativistic (SR) model. Note that relativity reduces the positive elastic energy $G(x)$ and increases the attractiveness of the spin-flip energies ϵ_n . This leads to negative SR formation enthalpies $\Delta H_n = \epsilon_n + G(X_n)$. Non relativistically, $\Delta H_n > 0$.

The same conclusions can be deduced from an " ϵ - G " decomposition [17] of the formation energies. Here, $G(x)$ is the configuration-independent elastic energy (analogous to VD) and ϵ_n is the "spin flip" energy (analogous to CT + REL). Figure 17 shows that in a non-relativistic description the positive $G(x)$ overwhelms the negative ϵ_n so the formation enthalpy $\Delta H_n = \epsilon_n + G(X_n)$ is positive. Relativity reduces the repulsiveness of $G(x)$ and enhances the

attractiveness of ϵ_n , thus leading to $\Delta H_n < 0$ and LRO.

The same method of analysis explains the trends in lattice-mismatch semiconductor alloys (Sec. VI). In fact, non-relativistic NiPt is analogous to size-mismatched semiconductor alloys, where $\epsilon_n < 0$ leads to SRO (Fig. 9), but the overwhelming role of $G(x) \gg 0$ leads to positive formation enthalpies $\Delta H_n = \epsilon_n + G(X_n)$ (Fig. 11b) and a phase-separating behavior (Fig. 8). The main contribution to stabilizing, $\epsilon_n < 0$ in semiconductors is lattice relaxation (Fig. 10). This leads to a negative ordering energy $\delta E_{\text{ord}} < 0$ for the chalcopyrite structure (Fig. 11b), despite $\Delta H_f > 0$.

To summarize, this section demonstrated how the cluster expansion can be used not only to predict novel structures, but also to analyze the *electronic origins of stability*.

VIII. APPLICATION TO BINARY COPPER ALLOYS AND TO Ni-Al

The intermetallic systems Cu-Au, Cu-Pd, Cu-Pt, and Cu-Rh form an interesting set in that while in elemental form, Cu, Pd, Pt, and Rh are all fcc metals, their 50%-50% equimolar compounds exhibit at low temperatures a range of structural symmetries [42,54-57]: CuAu has the fcc-based ($L1_0$) structure, CuPd has a bcc-based (B2) structure, CuPt has a rhombohedral ($L1_1$) structure, and CuRh does not exist (it phase separates into pure Cu + Rh). We have applied the CE method to these systems [28] in a parallel way to what was described earlier for the Pt systems. For Cu-Pd and for Ni-Al we also do a parallel CE for fcc vs bcc structures.

Figure 18 depicts the ground-state lines for the Cu-based alloy systems studied here and for Ni-Al (whose energies are calculated by the LMTO method). The symmetries established clearly from experiment [42,54-57] are also found theoretically, even though we have purposely omitted from the basis set used to extract J_F some of the structures which are *known* to be ground states. The results are as follows:

- **CuPt:** We find for CuPt (Fig. 18c) the established Cu_3Pt ($L1_2$) and CuPt ($L1_1$) phases, i.e., we correctly describe the competition between rhombohedral ($L1_1$) and tetragonal ($L1_0$) symmetries. Two additional ground-state fcc compounds Cu_7Pt ("D1") and CuPt_7 ("D7"), having twice the primitive fcc lattice vectors are also identified; these structures were not included in the "basis set" as they were unsuspected by the normal method of guessing to be ground states. We tested our prediction by calculating the energy of Cu_7Pt (D1) directly from LAPW (finding $\Delta H_f = -65.5$ meV/atom), confirming the cluster expansion prediction ($\Delta H_f = -61.5$ meV/atom). Indeed an early [58] investigation did propose the existence of the CuPt_7 ("D7") structure on the basis of electric measurements (however, this was not directly confirmed by x-ray studies).
- **CuPd:** Our calculated results [Fig. 18(b)] for CuPd show the observed fcc-type Cu_3Pd ($L1_2$) and bcc-type CuPd (B2) structures, indicating that our theory correctly reproduces the delicate balance between fcc and bcc interactions. The cluster expansion also predicts that

CuPd₃ (L1₂) and CuPd₇ (D7) are only ~3 meV/atom below the line connecting B2 ($x = 1/2$) with Pd ($x = 1$), hence, could form at low temperatures.

- **CuAu:** Our calculation [Fig. 18(a)] for CuAu correctly identifies Cu₃Au (L1₂), CuAu (L1₀), and CuAu₃(L1₂) to be on the ground state line (GSL). The Cu₃Au and CuAu structures are found to be very stable. On the other hand, the CuAu₃ is less stable: it moves above the GSL, when the structural relaxation is incorporated. This is consistent with the experimental fact that other structures can effectively compete with CuAu₃ at low temperatures.
- **CuRh:** Experimentally [42,54-57], Cu_{1-x}Rh_x exhibits fcc disordered solid solutions above 1150°C. At lower temperatures, the phase field exhibits a wide miscibility gap corresponding to phase separation into Cu-rich and Rh-rich fcc alloys. Our calculation for CuRh shows indeed a trivial horizontal GSL (not shown in Fig. 18) representing phase separation, as observed.
- **AlNi:** Experimentally [42,54-57], Al_{1-x}Ni_x shows both fcc- and bcc-based structures. The presence of the CsCl (B2) structure at $x = 1/2$ and the L1₂ structure at $x = 3/4$ well

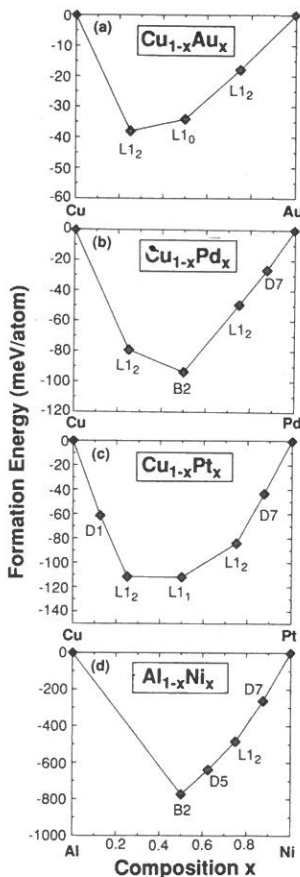


Figure 18. Ground-state line for (a) Cu_{1-x}Au_x, (b) Cu_{1-x}Pd_x, (c) Cu_{1-x}Pt_x, (d) Cu_{1-x}Rh_x and (e) Al_{1-x}Ni_x. From Ref. [28].

established. In addition, a bcc-like Al₃Ni₅ structure has been identified recently at low temperatures at $x = 5/8$ [57b]. It is isotypical with Ga₃Pt₅. Our calculations are shown in Fig. 18(d). The presence of the cubic CsCl structure (B2) and the NiAl₃ (L1₂) phase in the ground state are correctly reproduced. These are very stable phases with properties studied by many authors [54]. At $x = 5/8$ we find the D5 structure (Ga₃Pt₅-like) in the GSL. It is barely below the line joining the B2 and L1₂ points in Fig. 18(d), which means that, if truly a stable phase, it exists only at lower temperatures. True Ga₃Pt₅ has an orthorhombic distortion which we have not considered, but which could lower its energy still further. At $x = 7/8$ we predict the fcc-based configuration denoted D7, whose stability is not an experimental fact. In addition to these ground-state structures we have identified other metastable structures whose

energies are not far from the GSL. For example, our calculations place the DO_{22} configuration just 2.2 meV above the ground state at $x = 3/4$, while the DO_3 energy is further above. At $x = 3/4$ we find the DO_{23} structure just 1.3 meV above the $L1_2$ structure: it can be characterized as an $Al_5Ni_1Al_1Ni_1$ superlattice along the [410] direction. It is hence an intermediate structure between $L1_2$ and DO_{22} with ordering vector [201]. Finally, at $x = 5/6$ we found a configuration just 0.9 meV above the GSL. It is a $Al_5Ni_3Al_1$ superlattice along the [531] direction. The recent CPA-based calculation on Ni-Al [59] produces formation energies (ibid, Table 2) that are 2-3 times smaller in magnitude than our direct *ab-initio* results. This could be due to the neglect of charge-transfer (CT) in their calculation [compare the CPA and the present Madelung energies in Fig. 3 and in Eq. (22)]. Testing awaits inclusion of CT in CPA.

Figure 16(a) gives the observed [42,54] Ni-Al phase diagram; the calculated fcc and bcc solid phase portions of the $Al_{1-x}Ni_x$ phases diagram is given in Fig. 16(b). The lines of equilibrium are cut at $T = 1640$ K where melting begins. The binodal of B2- $L1_2$ and $L1_2$ -Ni equilibrium lines agree well with experiment at temperatures near melting. At lower temperatures the B2- $L1_2$ binodal is deformed by the occurrence of the Al_3Ni_5 phase D5, which we find to be stable below 950 K. The experimental phase diagram near the onset of the D5 stability is not well reproduced by our calculation, but does not differ much from it. Thus, the onset of the D5 stability marks the appearance of a new parameter of order in the B2 medium. At lower temperatures, our $L1_2$ -Ni binodal falls faster (vertically) than experiment, due to the presence of the stable $AlNi_7$ phase (D7) in our calculations. This phase has never been reported, but the observed instability of the binodal might be indicating the presence of a hidden phase like our D7. Since this phase has a very low Al concentration, and since its translation vectors are fcc-like (but doubled), this phase might be easily confused with fcc Ni with a random distribution of Al impurities.

IX. THE ROLE OF ATOMIC RELAXATIONS

A. When Is Relaxation Expected to Be Important

As we have seen, the utility of the CE is largely determined by its rate of convergence. For systems with inherently short-ranged interactions, such as chemical interactions in size-matched alloys [13] or magnetic exchange interactions in spin alloys [4,5], the CE can be applied easily—requiring ≤ 10 interactions. But when A and B have very different sizes, then changing the occupancy of some sites of a given configuration will cause the atoms to relax from their original lattice positions, leading to changes, ΔE_{REL} in the formation enthalpy (Table III) and ordering energy [Eq. (28)]. For example, replacing a small atom by a larger one will cause its

immediate neighbors to relax outwards. The relaxation of the nearest neighbors can, in turn, cause a relaxation of their neighbors. This effect is cumulative: if several consecutive atoms are replaced by larger atoms, then the relaxation of their neighbors will be even greater. This does not pose a formal problem for the CE because Eqs. (1)-(7) can be applied to *any* quantity that is a unique property of the configurations of the system. (Different properties will, of course, have different J 's.) This includes the energy of any relaxed configurations, since this energy is a unique function of the unrelaxed configuration.

Indeed, cluster expansions for systems with lattice relaxation converge more slowly than cluster expansions for unrelaxed systems. This can be seen from the contribution of the relaxations to the pair interaction energies:

$$\Delta J_{i,j} = - \sum_{k,l} F(\vec{R}_i - \vec{R}_k) \cdot \Phi^{-1}(\vec{R}_k - \vec{R}_l) \cdot F(\vec{R}_j - \vec{R}_l), \quad (29a)$$

where $F(\vec{R}_i - \vec{R}_k)$ is the force on site \vec{R}_i induced by the atom at site \vec{R}_k ("Kanzaki force") [18,60] and $\Phi(\vec{R}_k - \vec{R}_l)$ is the force-constant matrix. In many systems the force constants decay slowly along particular directions, so the relaxations will propagate for long distances; such is the case for zincblende semiconductors, where the force constants decay slowly along the $\langle 001 \rangle$ bond chains [18].

One can develop a qualitative model showing when relaxation is expected to be important. Consider the simple relations $\omega \sim \sqrt{\Phi/M}$; $\Phi^{-1} \sim 1/(\langle \omega^2 \rangle M)$ and $\vec{F} \sim a^2 B [1/a \partial a / \partial x]$, where ω is the phonon frequency and $\sqrt{\langle \omega^2 \rangle}$ is its mean, M is the mass, $a(x)$ is the lattice constant, and $B(x)$ is the bulk modulus. Using these in Eq. (29a) leads to the scaling rule

$$\Delta J \propto \frac{a^4 B^2 (a_A - a_B/a)^2}{\langle \omega^2 \rangle M}. \quad (29b)$$

Hence, relaxation is important when (i) the relative size difference $(a_A - a_B)/a$ is large, (ii) the alloy is hydrostatically stiff (large B) but has (iii) low-energy phonons ($\langle \omega^2 \rangle$ small). Similar relations have recently been used by Beiden and Vaks [61] to illustrate that for TiV, TiCr, and CuZn the relaxation correction ΔJ is comparable to the unrelaxed J .

Since the term "relaxation" has, in the author's view, been used rather vaguely in the phase stability literature, I next attempt to define it more precisely, using a "sequential process". While the order of the sequence is chosen arbitrarily, it will nevertheless serve to clarify the basic elements of relaxation.

B. Decomposition of the Relaxation Process

We will decompose the excess energy at fixed volume of an AC/BC system. Here we generalize our previous notation to a *pseudo* binary alloy where the statistical variables are A/B,

as before, but an additional, fixed sublattice is occupied by the "common atom" C. This decomposition is identical to that of Sec. VII.D, except that here we identify the components of ΔE_{REL} . The purpose of this decomposition is to help us understand the role of relaxation in CEs; (our method of calculation does not, however, depend on this decomposition). We break ΔE as follows:

$$\Delta E(\sigma, V) = \Delta E_{\text{VD}}(x, V) + \delta E_{\text{UR}}(\sigma, V) + \delta E_{\text{C}}(\sigma, V) + \delta E_{\text{A,B}}^{\text{int}}(\sigma, V) + \delta E^{\text{ext}}(\sigma, V). \quad (30)$$

- The first term is the "volume deformation" (VD) energy of Sec. VII.D, i.e., the energy required to change the volume of AC from V_{AC} to V , and that of BC from V_{BC} to V :

$$\Delta E_{\text{VD}}(x, V) = (1 - x)[E(\text{AC}, V) - E(\text{AC}, V_{\text{AC}})] + x[E(\text{BC}, V) - E(\text{BC}, V_{\text{BC}})]. \quad (31)$$

Since ΔE_{VD} depends primarily on x and not on the individual configuration [8a], it affects neither the ordering temperature nor relative energies of configurations at a fixed composition. It could, however, determine whether or not an homogeneous ordered phase will decompose into its constituents.

- The second term, δE_{UR} , is the energy difference between the unrelaxed (UR) structure (all atoms at ideal lattice sites) and ΔE_{VD} . This is often termed the "spin-flip" energy. Classic Ising models [4] as well as the S-CPA based GPM and CW methods treat only this energy.
- The third term, δE_{C} , occurs only in *pseudo* binary alloys with a common sublattice. It is the energy gained when the common C atoms (P for GaP/InP) are relaxed, but the A and B atoms are held in their ideal positions. In a binary $A_{1-x}B_x$ system, where there are no common C atoms, there is no δE_{C} .
- The "cell internal" relaxation energy $\delta E_{\text{A,B}}^{\text{int}}$ is the energy gained when all atoms inside a unit cell are relaxed, but the unit cell is kept cubic. It corresponds to relaxation of the crystallographic degrees of freedom which are not determined by symmetry, e.g., the interplanar distances in $L1_1$. This relaxation is zero in certain high-symmetry structures, such as the A_1B_1 [001] superlattice (the $L1_0$ structure), the A_1B_3 [201] superlattice (DO_{22}), and the Luzonite A_1B_3 structures ($L1_2$).
- Finally, the cell-external relaxation energy δE^{ext} is the energy gained when the unit cell vectors are allowed to relax, e.g., the tetragonal c/a ratio in $L1_0$. This term vanishes by symmetry for the $L1_2$ structures. Note that ΔE_{REL} of Sec. VII.D is $\delta E_{\text{C}} + \delta E_{\text{A,B}}^{\text{int}} + \delta E_{\text{A,B}}^{\text{ext}}$.

*One may wonder why we treated ΔE_{VD} separately from $\delta E^{\text{int}} + \delta E^{\text{ext}}$ since the former represents a large energy *investment* that is partially *returned* once the A,B relaxation takes place. The answer is that ΔE_{VD} is configuration-independent while δE depends explicitly on σ . Hence, the ordering energy of Eq. (26) and T_c do not depend on ΔE_{VD} , but they do depend on δE [viz., Eq. (28)].

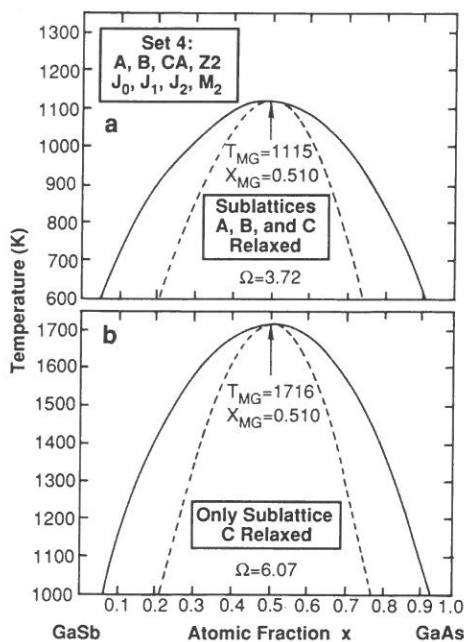


Figure 19. Effect of relaxation on the calculated phase-diagram and mixing enthalpy parameter Ω of $(\text{GaSb})_x (\text{GaAs})_{1-x}$. Note that relaxation of the As + Sb sublattices reduces the miscibility gap temperature from 1716 K to 1115 K. The mixing-enthalpy parameter (in Kcal/mole) is defined as $\Delta H_{\text{mix}} = \Omega x(1-x)$ and is reduced from 6.07 to 3.72. From ref [8a].

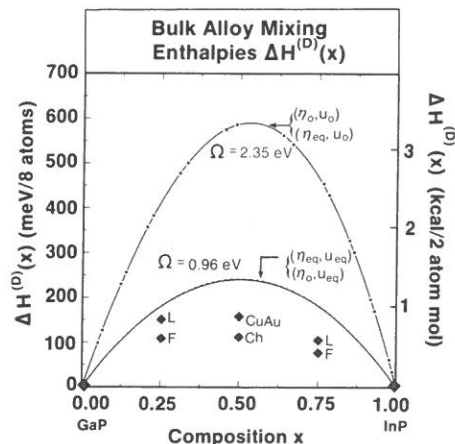


Figure 20. Effect of relaxation on the mixing enthalpy of $(\text{GaP})_x (\text{InP})_{1-x}$. Here $\eta = c/a$ (cell-external) and u measures the cell internal relaxation. (u_o, η_o) denotes unrelaxed; (u_{eq}, η_{eq}) denotes relaxed. The mixing-enthalpy interaction parameter (in Kcal/mole) is defined as $\Delta H_{\text{mix}} = \Omega x(1-x)$. Diamond-like symbols shows results for ordered structures using the notation of Table II.

C. Manifestations of Relaxations

There are numerous experimental and theoretical manifestations of the effects of relaxation on phase stability:

(i) Relaxation in alloys is an experimental fact. Both cell-internal and common-sublattice relaxations are clearly seen in EXAFS studies of pseudobinary $(\text{AC})_{1-x}(\text{BC})_x$ semiconductor alloys [62] that show that the A-C and B-C bond lengths were closer to the bond lengths in pure AC and pure BC than to the average bond length of the alloy. This is also illustrated by the calculation of Fig. 10. Cell-internal relaxation was also demonstrated recently by EXAFS studies in binary metal systems, e.g., $\text{Ni}_{1-x}\text{Au}_x$ [63] where distinct, non-VCA Ni-Ni; Ni-Au and Au-Au bond lengths are seen. Off-site atomic displacements further lead to distinct asymmetric diffuse scattering of x-rays and neutrons.

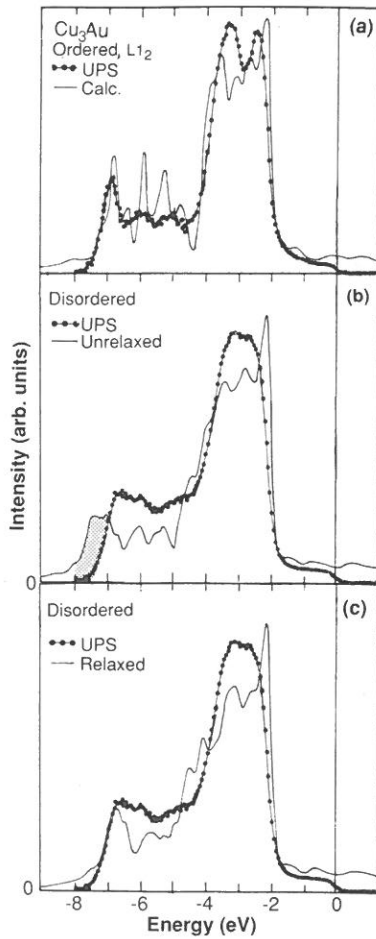


Figure 21. Comparison between our fully relativistic DOS and the measured valence band photoemission (UPS) for Cu_3Au . The thin lines represent the calculated results, while the connected dotted lines represent the experimental results. (a) The ordered $L1_2$ Cu_3Au . (b) The unrelaxed $\text{Cu}_{0.75}\text{Au}_{0.25}$ DOS. (c) The relaxed $\text{Cu}_{0.75}\text{Au}_{0.25}$ DOS. The shaded area in (b) highlights the ~ 1 -eV discrepancy with experiment, which is rectified by including relaxation (c). From ref [30].

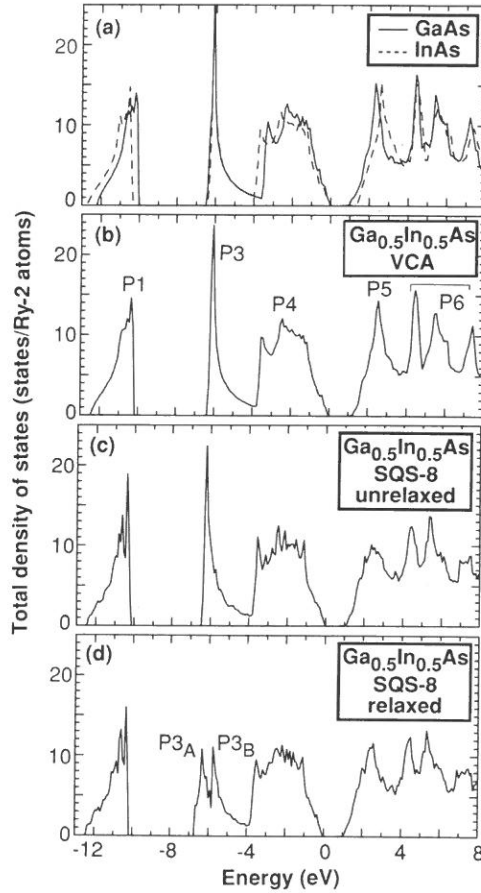


Figure 22. Total DOS of the GaAs-InAs system. (a) Binaries at the unrelaxed alloy equilibrium lattice constant $\bar{a} = 5.80\text{\AA}$, (b) VCA, at the same lattice constant, (c) unrelaxed, and (d) relaxed. Note in (c) and (d) the relaxation-independent splitting in the P1 region (absent in the VCA) and the relaxation-induced splitting in the P3 region (absent in CPA). From ref. [66].

(ii) Volume-deformation (ΔE_{VD}) effects can determine whether or not an homogeneous ordered phase will decompose into its constituents. Neglect of ΔE_{VD} [52] can lead to the wrong sign for the formation energy and wrong conclusions on ordering, as shown in Ref. [29]. Furthermore, previous phase-diagram calculations on Cu-Au [17] have shown that inclusion of volume deformation narrows significantly the single-phase domains while broadening the phase-coexistence regions. Simple Ising models miss this effect.

(iii) δE_C is the dominant energy-lowering mechanism in size-mismatched semiconductor alloys. Calculations [8,24,64] show that it lowers the miscibility gap temperature by a few hundred degrees (Fig. 19), and the mixing enthalpy by more than a factor of two (Fig. 20).

(iv) Cell-internal relaxations δE^{int} can have a profound effect both on the short range order (underlying δE_{ord}) and on the LRO. Table III shows for example that (in a non-relativistic description) NiAu has $\delta E_{\text{ord}}(L1_0) < 0$ in the absence of relaxation. In contrast, when relaxation is permitted one finds $\delta E_{\text{ord}}(L1_0) > 0$ (since the random alloy relaxes more than the ordered $L1_0$ structure). Hence, ordering is predicted in the absence of relaxation, while inclusion of relaxation leads to the prediction of phase-separation. In general the cell-internal relaxation energy depends strongly on the symmetry of the structure: ΔE_{REL} for the $L1_0$, $L1_1$, and the $Z2$ structures are -20.2, -28.0, and -177.8 meV/atom in NiAu, and -18.0, -24.5, and -134.0 meV/atom in NiPt [51].

(v) Cell-external relaxation δE^{ext} can have a decisive effect on phase stability: c/a relaxations can decide the relative stability of the $L1_2$ structure (for which $c/a = 1$ by symmetry) and the DO_{22} structure (for which $c/a \neq 1$ is allowed by symmetry). This is the case for some transition metal alluminides [65].

(vi) Relaxation can cause large, ~ 1 eV energy shifts in the density of states. This is illustrated in Fig. 21 for $\text{Cu}_{0.75}\text{Au}_{0.25}$ [30] and in Fig. 22 for the semiconductor alloy $\text{Ga}_{0.5}\text{In}_{0.5}\text{As}$ [66]. Note that relaxation displaces the deep -7 eV bonding states of $\text{Cu}_{0.75}\text{Au}_{0.25}$ by ~ 1 eV to lower binding energies, thus removing the main disagreement with UPS data. In $\text{Ga}_{0.5}\text{In}_{0.5}\text{As}$ (Fig. 22) it leads to a pronounced splitting of the cation s-band at ~ -6 eV to In-derived and Ga-derived peaks, $P3_A$ and $P3_B$, respectively.

Clearly, relaxation has profound effects on phase stability, phase diagrams, and the electronic structure. Unfortunately, it was neglected in many previous methods, as discussed next.

D. How Was Relaxation Treated in Previous Cluster Expansions

The recognition of the "atomic size factor" is as old as structural chemistry and physical metallurgy, and is clearly reflected in the thinking of Pauling, Hume-Rothery, Pearson, Darken and Gurry, Miedema, and others. Despite that, there is, in my view, a great deal of confusion in the current literature in relating the "size factor" to "relaxation". This is illustrated by the often posed question "what is meant by atomic size (in a crystal)," and by incorrect statements such as "if an alloy obeys Vegard's rule, relaxation must be negligible" or "in a random alloy, relaxation is averaged out." We saw in Eq. (29b) that relaxation exists if there is an $|a_A - a_B| \neq 0$ size mismatch, whether Vegard rule is obeyed or not. Furthermore, relaxation exists even in a configurationally-averaged random alloy, simply because it is not the atomic *geometry* that is being averaged, but the *energies* of the differently relaxed configurations. Hence, relaxation

survives configurational averaging (cf. Fig. 10). Finally, our inability to uniquely define "atomic size" in a multi-component system should not be confused with the fact that atoms generally do not reside on the idealized, mathematical lattice points. In fact, the *propensity* of atoms to select certain local chemical environments is *manifested* by relaxation. Hence, since relaxation can be measured and calculated, I will focus on it, rather than on its metaphorical *cause* ("size factor") which involves model assumptions on apportioning a measured bond length into rigid atomic radii of the constituents.

With this in mind, let me use the decomposition of the relaxation outlined in Sec. IX B to review how previous works treated relaxation within the CE.

(i) The CPA-based "concentration wave" and "Generalized Perturbation Method" [19-23,52,67a], neglected all forms of relaxation. Practical methods, enabling inclusion of all forms of relaxation in these otherwise successful approaches must be developed. Furthermore, since relaxation is an experimental fact, it would be interesting to understand in detail the mechanism that lead in these previous calculations to the often cited agreement with experimental phase diagrams and diffuse scattering in size mismatched alloys despite the neglect of relaxation.

(ii) In previous (5-structure) Connolly-Williams cluster expansions [7,25-27] only high-symmetry short-period structures were used as input, so the important effects of $\delta E_{A,B}^{\text{int}}$ and δE^{ext} went unnoticed.

(iii) Many approaches use the unit cell volume or some "sublattice volumes" V_A and V_B [67b] as the central external parameter, so they just include the hydrostatic volume relaxation. This is done either by using volume-dependent interaction energies [7,24-27] or by adding an $\Omega x(1-x)$ term to the CE [17]. None of these techniques, however, captures the effects of sublattice relaxation, i.e., δE_C and $\delta E_{A,B}^{\text{int}}$, which are *cell-internal* relaxations.

(iv) A number of calculations on semiconductor alloys [24,68] included δE_C , but neglected all or part of $\delta E_{A,B}^{\text{int}}$.

(v) A recent calculation on $\text{Cu}_{1-x}\text{Au}_x$ included δE^{ext} , but neglect cell-internal relaxations [14].

(vi) Calculations that incorporate all terms of Eq. (30) (but with certain limitations on the symmetries of the structures) include Refs. [8,13,18,28-32,51].

E. Effects of Relaxation on Convergence of the Cluster Expansion

Many of the examples cited above demonstrate that relaxation has some quantitative effects on calculated properties. I next demonstrate how ignoring relaxation can lead to a qualitative failure. The case in point is coherent superlattices. To illustrate this effect we construct a CE, using as input $N_G = 20$ ordered structures for AC = GaP and BC = InP. We calculated their fully relaxed formation energies $\Delta H_f(\sigma)$ [Eq. (6)] with the "valence force field" (VFF) model [69],

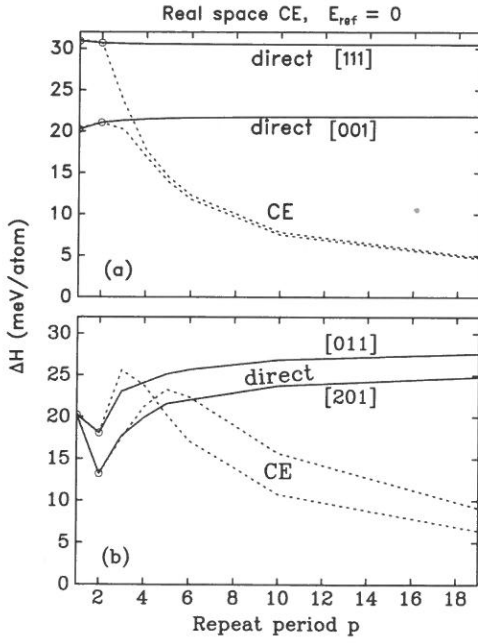


Figure 23. Formation energies for GaP/InP superlattices as a function of repeat period p and of superlattice direction. Solid lines are direct results calculated with the VFF model. Dashed lines are results of a real-space cluster expansion of the VFF energies using a set of input structures with $p \leq 2$, and interaction energies J_0, J_1, J_3, J_4 , and the first seven pair interactions. The correct formation energy for long periods (solid lines) tends to a constant energy that is a function of direction, but the cluster expansion results (dashed lines) tend to zero for all directions. From ref [70].

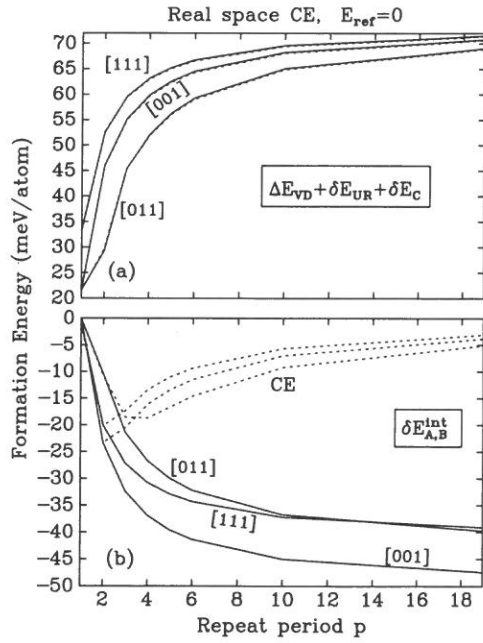


Figure 24. (a) Formation energies for GaP/InP superlattices as a function of repeat period, p , when only the common P atoms are allowed to relax. (b) Energy gained when the Ga and In atoms are also allowed to relax (cell internal AB-relaxation energy). Solid lines are results calculated with the VFF model. Dashed lines are results of a cluster expansion of the VFF results for a set of input structures with $p \leq 2$, and interaction energies J_0, J_1, J_3, J_4 , and the first seven pair interactions. From ref [70].

and obtained [70] the interaction energies from Eq. (7). Figure 23 contrast the *predictions* [Eq. (3a)] of this CE (dashed lines) with the results of direct calculations [Eq. (6), solid lines] for the formation energies of $(\text{GaP})_p(\text{InP})_p$ with $1 \leq p \leq 20$. The VFF results for $p = 1, 2$ (circles) were used to fit the J 's of the CE; the CE energies for $p \geq 3$ are pure predictions. Note that the CE begins to fail even for $p = 3$. Including structures with periods 3 and 4 in the fit delays the failure of the CE to longer periods, but direct calculations for longer period superlattices can be very expensive. The most disturbing feature of Fig. 23 is that it fails completely for long-period superlattice limit. The true long-period limit for the formation energy of a coherent superlattice in the direction \hat{G} is the constituent strain (CS) energy [71] of the two components: $\Delta H(p = \infty, \hat{G}) = \Delta E_{\text{CS}}(\hat{G})$, while the CE converges to a \hat{G} -independent constant as $p \rightarrow \infty$.

To see how the various components of the relaxation energy of Eq. (30) affect this behavior, we have constructed a CE from each individual relaxation energy term (Fig. 24). We find that

the cluster expansion works perfectly well for the unrelaxed lattice: δE_{UR} is captured in this case almost exactly by a single nearest neighbor pair interaction. δE_C is the dominant relaxation for short-period superlattices, but it vanishes as $p \rightarrow \infty$. It too is very accurately represented by a short-ranged CE with only four pair interactions. This is illustrated in Fig. 24(a), which shows direct and CE energies for $\Delta E_{VD}(x,V) + \delta E_{UR}(\sigma,V) + \delta E_C(\sigma,V)$ for superlattices as a function of p . The figure also shows that the CE captures this energy almost exactly. The long-period limit of this quantity is ΔE_{VD} for all superlattice directions. The dominant form of relaxation for medium- and long-period superlattices is $\delta E_{A,B}^{int}$, but, as shown in Fig. 24(b), this term is not properly represented by the CE, which predicts $\delta E_{A,B}^{int} = 0$ as $p \rightarrow \infty$. (This feature depends on the order in which cell-internal A,B relaxation and common-atom relaxation is performed.) In any event, a finite-ranged CE is completely incapable of capturing either the concerted relaxation that determines the strain energy or the directional dependence that it causes; it predicts $\Delta H \rightarrow 0$ as $p \rightarrow \infty$.

The long-period superlattice problem is intrinsic to the CE, in that any finite cluster expansion will predict that the coherent superlattice formation energy goes to zero in the long-period limit. The reason for this failure is simple: the CE sees all A atoms that are far from the interface as if they were in a bulk A crystal, since the figures of a finite CE connect them exclusively to other A atoms. Similarly, the CE treats almost all B atoms as bulk B. As a result, the formation energy per atom in the long-period superlattice limit of the CE is zero—the formation energy of both bulk A and bulk B—and the CE completely misses the constituent strain present in coherent superlattices.

Another way of seeing how relaxation mandates long range interactions in a cluster expansion was illustrated to me by a question asked by M. Sluiter. Consider a system that orders in a tetragonally-deformed ($c/a \neq 1$) structure (e.g., DO_{22}) below T_c , and has a disordered cubic ($c/a = 1$) phase with strong SRO above T_c . The existence of strong SRO in the disordered phase implies that the first few $\bar{\Pi}_F$'s are rather similar below and above T_c . Were we to stop the CE after a few $\bar{\Pi}$'s, the configurational internal energies of the ordered and disordered phases would be very similar. Yet, we know that these phases have different c/a ratios, so something must be missing in the CE which fails to recognize this fact. The answer is that the two phases are distinguished by their medium and long range $\bar{\Pi}_F$'s so, by implication, a proper description of relaxed configurations requires inclusion of many J_F 's. One might try and fix this problem by splitting the degeneracy factor D_F of the figures [Eq. (2)], e.g., use different J_F for the parallel and perpendicular directions. Since this will have to be done for *all* superlattice orientations, it will require many total energy calculations and many J 's. *Our foregoing discussion highlights the main drawback of the cluster expansion: in the presence of relaxation the series converges slowly!* I next demonstrate how an ordinary long range CE can be constructed instead, using as input the total energies of 10-20 ordered configurations. This addresses the two questions raised

by S. C. Moss in his summary talk, namely "How to (a) incorporate properly strain in the theoretical calculation of local order and phase stability, and (b) derive it from first-principles electronic calculations of alloy structure."

X. RECIPROCAL SPACE CLUSTER EXPANSION

In this section we will show that a reciprocal space CE provides an effective way to deal with systems that have slowly converging cluster expansions. The basic idea [70] of the reciprocal space expansion is to replace the individual real-space interaction energies J_F , where the interaction energy of one figure has no relationship with the interaction energy of any other, with a single reciprocal space function, $J(\vec{k})$, on which we impose a smoothness condition, which minimizes the gradient of $J(\vec{k})$. Using this construction lets the CE select the important figures, and we are not limited by $N_F = N_\sigma$ as in the real-space Connolly-Williams approach [Eq. (8)]. Furthermore, the singular $J(\vec{k} = 0)$ term causing the failure of the CE for long period superlattices, will be treated separately. Since a sum over only a few \vec{k} -points of $J(\vec{k})$ corresponds to an infinite series in real space, this series will correctly predict the energies of arbitrary relaxed configurations.

A. Maximum-Smoothness Constraint in the Reciprocal-Space Representation

To recast the CE in reciprocal space, we first Fourier transform the spin products:

$$S(\vec{k}, \sigma) = \frac{1}{N} \sum_1^N S_1(\sigma) e^{i\vec{k} \cdot \vec{R}_1}, \quad (32)$$

and the inverse transform is

$$S_1(\sigma) = \sum_{\vec{k}} S(\vec{k}, \sigma) e^{-i\vec{k} \cdot \vec{R}_1}, \quad (33)$$

where the sum over \vec{k} in Eq. (33) runs over the first Brillouin Zone and \vec{R}_1 denotes unrelaxed lattice site positions. The $S(\vec{k}, \sigma)$ functions have a very useful feature: for an ordered configuration σ , $S(\vec{k}, \sigma)$ will only be non-zero for a finite set of points \vec{k} . In particular, the only \vec{k} -points that can have $S(\vec{k}, \sigma) \neq 0$ are $\vec{k} = 0$ and the \vec{k} -point that are reciprocal

lattice vectors of the unit cell of σ . In the following, we choose the coordinate system such that one of the lattice sites is at the origin, and we label that site $\vec{R}_0 = 0$. We will use the definition of $S(\vec{k}, \sigma)$ to transform the part of the CE energy due to the pair interactions [third term on the right-hand-side of Eq. (1)]. By defining

$$J(\vec{k}) = \frac{1}{2} \sum_n^N J_{0,n} e^{i\vec{k} \cdot \vec{R}_n} \quad (34)$$

using the convolution theorem and averaging over the point group, we arrive, at

$$E_2(\sigma) = N \sum_k J(\vec{k}) |S(\vec{k}, \sigma)|^2. \quad (35)$$

We have replaced the sum over an infinite set of real-space pair interactions with a sum over a few \vec{k} -points. This is the "concentration wave" representation of Khachatryan [60]. While three-body and higher figures could also be described by a reciprocal-space expansion, the formulae are too complicated for practical use. Instead three-body and four-body figures will be added as explicit real space figures:

$$E_{CE}(\sigma) = N \sum_F' D_F J_F \bar{\Pi}_F(\sigma) + N \sum_k J(\vec{k}) |S(\vec{k}, \sigma)|^2, \quad (36)$$

where the primed sum runs over the set of non-pair figures included in the expansion.

Since the reciprocal space expansion up to this point is equivalent to a real space expansion, the two forms share the same problems. In particular, the total number of figures N_F included in Eq. (7) or Eq. (36) must be less than the number of structures N_σ whose energies are used to fit J_F and $J(\vec{k})$. To this end we deviate from Khachatryan's concentration wave method in two ways. First, $J(\vec{k})$ will be calculated from the local density theory (much like in the Connolly-Williams approach), not from elasticity theory. Second, we require that $J(\vec{k})$ be a smooth function of \vec{k} , thus assuring that any number of figures can be included, and that the interactions fall off at large interatomic separations.

We define a "smoothness value" M as

$$M = \frac{1}{\alpha} \sum_k J(\vec{k}) \left[-\nabla_k^2 \right]^{\lambda/2} J(\vec{k}) = \frac{N}{2\alpha} \sum_I R_I^\lambda D_I J_I^2, \quad (37)$$

where R_I are interatomic distances to shell I , the exponent λ is a free parameter, and α is a

normalization constant:

$$\alpha = \frac{N}{2} \sum_I R_I^\lambda D_I . \quad (38)$$

The smoothness condition is achieved by minimizing M through a Lagrange multiplier. It is equivalent to requiring that the pair interactions fall off rapidly for large distances. Our use of this smoothness condition will be tested when we examine the quality of predictions made using the function $J(\vec{k})$.

Our fitting procedure will be to solve

$$\sum_{\sigma} \omega_{\sigma} |E_{\text{direct}}(\sigma) - E_{\text{CE}}(\sigma)|^2 + tM = \text{Minimum} \quad (39)$$

by varying $\{J_F\}$ (for the non-pair figures included in the expansion) and $\{J_I\}$ (for the pair figures). Here $E_{\text{direct}}(\sigma)$ is the directly calculated *and fully relaxed* energy [Eq. (6)], $E_{\text{CE}}(\sigma)$ is defined in Eq. (36), and t is a scaling factor. The function $J(\vec{k})$ appearing in Eq. (36) is represented by symmetrized plane waves, thus interpolating between those values of \vec{k} included in the set of input structures. The scaling factor is a matter of choice, but we have found in tests that any value in the range $1 \leq t \leq 100$ produces almost identical results. Unless otherwise indicated, we will use $t = 1$. Note that using $t = 0$ completely eliminates the smoothness condition, and results in a plain real space fit of Eq. (7). If we fit with a large number of figures and $t = 0$, the fitting procedure has no way of knowing which interactions are short-ranged and which are long-ranged. As a result, the long-ranged interactions will be as strong as the short-ranged interactions, which appears unphysical. The chief advantage of the reciprocal space method is that it lets the fitting procedure choose which pairs are important. Because of the smoothness criterion, any pair figure that is not strictly necessary for a good fit will have an interaction energy of zero. Also, the smoothness criterion naturally favors short-ranged over long-ranged interactions, which is physically sensible. The maximum smoothness condition does not solve the long superlattice problem noted in Figs. 23 and 24. This will be fixed shortly.

B. Tests of Reciprocal Space Cluster Expansion

We are now ready to apply the reciprocal space CE. As in Sec. IX.E, we will use the VFF model to calculate the energies $E_{\text{direct}}(\sigma)$ of different structures for the GaP/InP system. To examine the convergence of the CE we will use four different sets, $s_0 \subset s_1 \subset s_2 \subset s_3$, of input structures for the calculations. These sets are (see Table II and Fig. 5)

$$\begin{aligned}
s_0 &= \{A, B, CA, L1, L3\} && (5 \text{ elements}), \\
s_1 &= s_0 \cup \{CH, CP, Z2\} && (8 \text{ elements}), \\
s_2 &= s_1 \cup \{V2, Y2, W1, W3\} && (12 \text{ elements}), \text{ and} \\
s_3 &= \text{all structures in Table II} && (27 \text{ elements}).
\end{aligned}$$

The set s_0 is the standard Connolly-Williams set [7], while the set s_1 was previously used in real space fits for many semiconductor alloys [8]. Set s_3 was previously used in a real space CE of semiconductor band gaps [32].

To test the reciprocal space versus real space CE, we will solve Eq. (39) to determine the interaction energies, using each input set s_0 , s_1 , s_2 , and s_3 . For each input set, we then predict the total energies of a large set of *new structures*, none of which are used in the fit. The predictions are performed for four types of structures: (i) long-period superlattices: $(\text{GaP})_p(\text{InP})_p$ superlattices with $3 \leq p \leq 6$ and $p = 10$ in the [001], [011], [111], and [201] directions (20 structures), (ii) intermixed superlattices: superlattices with $p = 1, 2$ in which some of the atoms on each side of the interface have been swapped—thereby lowering the symmetry (24 structures), (iii) $x \neq 1/2$ structures: structures in which the composition is $x \neq 1/2$. These structures consist of $(\text{GaP})_p(\text{InP})_q$ superlattices, with $p \neq q$, e.g., $(\text{GaP})_1(\text{InP})_6$ and $(\text{GaP})_6(\text{InP})_1$ superlattices. We also include here substitutional impurities, i.e., GaP (InP) supercells with 8, 16, 32, and 64 atoms, containing a single In_{Ga} (or Ga_{In}) substitutional impurity (43 structures). Our final test case is (iv) large supercell simulations of random alloys: the energy of a random $\text{Ga}_x\text{In}_{1-x}\text{P}$ alloy is determined by averaging over many different randomly generated configurations of a fully-relaxed 1000-atom supercell [72]. For each of the new structures in (i)-(iv), we independently calculate the VFF formation energy and compare it with the CE prediction. The calculated formation energies for sets (i)-(iii) cover a wide range: $17.7 \rightarrow 30.6$, $14.9 \rightarrow 32.2$, and $2.2 \rightarrow 31.0$ meV/atom, respectively.

We perform the CE in three different ways, shown in panels (a)-(c) of Fig. 25. In all cases, we use the following real-space interactions in the first term of Eq. (36): J_0 , the empty figure (i.e., a constant term that is independent of σ), J_1 , a single site term, J_3 the nearest-neighbor three-body interaction, J_4 , the nearest-neighbor four body interaction. Our first calculation (a) is a simple real space CE using the first seven pair figures, where the number of pair figures is adjusted to assure that $N_\sigma \geq N_F$ for set s_0 . In our second calculation (b), we repeat the same real space expansion, but expand $E - E_{\text{ref}}$ in place of E . We use the volume-deformation energy $\Omega x(1-x)$ for E_{ref} . The value of Ω is treated as a fitting parameter, and we find $\Omega = 147.1$ meV/atom, using input set s_2 . Finally (c), we repeat the latter CE, but this time using the reciprocal space formalism, i.e., we set $t = 1$ instead of $t = 0$ in Eq. (39), and we include the

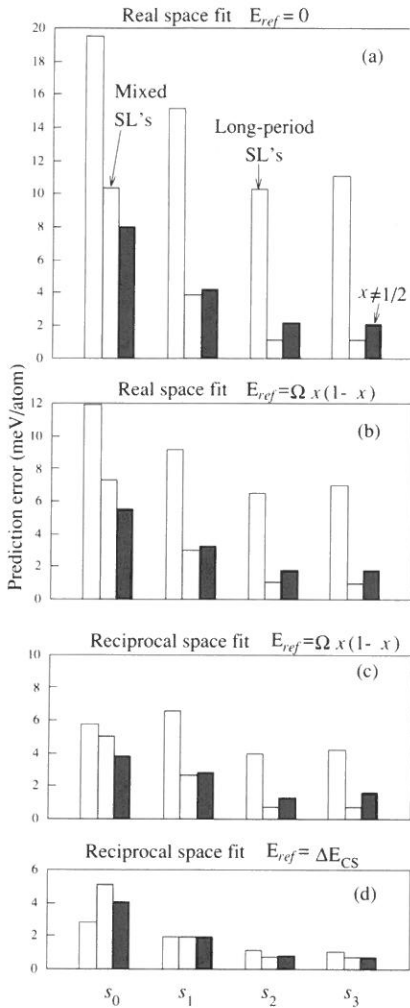


Figure 25. Prediction errors for different CE's of GaP/InP. The CE is applied to $E - E_{\text{ref}}$ for four different fitting procedures: (a) Real-space fit with $E_{\text{ref}} = 0$ and $N_p \leq 7$. (b) Real-space fit with $E_{\text{ref}} = \Omega x(1-x)$ and $N_p \leq 7$. (c) Reciprocal-space fit with $E_{\text{ref}} = \Omega x(1-x)$ and $N_p = 20$. (d) Reciprocal-space fit with $E_{\text{ref}} = \Delta E_{\text{CS}}$ and $N_p = 20$. Prediction errors are shown separately for long period superlattices (open rectangles), intermixed superlattices (shaded rectangles), and structures with $x \neq 1/2$ (solid rectangles). Each CE is repeated using the input sets s_0 , s_1 , s_2 , and s_3 (defined in text). Real space fits have the scaling parameter $t = 0$, while reciprocal space fits have $t = 1$ [Eqs. (39) and (45)]. From ref [70].

first twenty pair interactions. The fitted value of Ω is 129.5 meV/atom, using s_2 .

In Fig. 25(a-c), we present the root mean square (rms) prediction error of the CE's for each of the three sets of new structures. Table IV summarizes the results. Note that the interaction energies were fitted without any knowledge of the energies of these new structures.

We note the following trends: (i) For the intermixed structures, we see that using set s_2 of 12 input structures is adequate for making accurate predictions for all three methods. (ii) Using $E_{\text{ref}} = \Omega x(1-x)$ works better than using $E_{\text{ref}} = 0$. (iii) The reciprocal space expansion works better than the real space expansion. Another indication of the superiority of the reciprocal space expansion is the *maximum* error made in the CE predictions—which is a measure of how well CE predictions can be trusted. (A CE that predicts the energy 95% of structures exactly, but has a large prediction error for the remaining 5%, will have a small rms "prediction error", but is not worth much because we can never be sure whether the prediction for a new structure belongs to the 95% or the 5%.) Table IV shows both the rms and the maximum prediction error of the three fitting procedures using input set s_2 . The reciprocal space fit (c), having much smaller maximum errors, is clearly superior to the real space fit. (iv) The predictions for the formation energy of the random alloy, using input set s_2 , are 19.90, 20.95, and 20.77 meV/atom, for the three fitting procedures (a)-(c). The directly calculated formation energy for the random alloy using the 1000 atom simulation is 20.45 meV/atom. Hence, all methods predict the energy of the random alloy rather well. Finally, (v) as discussed above, all

Table IV. Root mean square (rms) and maximum (max) prediction errors for different cluster expansions of GaP/InP. Errors are reported separately for long-period superlattices, intermixed short-period superlattices, and for structures with composition $x \neq 1/2$. The input set s_2 was used for each CE. Real-space figures J_0, J_1, J_3 , and J_4 were included in each CE. Lines (a), (b), (c), and (d) refer to the CE's described in panels (a), (b), (c), and (d), respectively of Fig. 25. All energies are in meV/atom.

	Cluster expansion		Long-period SL's		Intermixed SL's		$x \neq 1/2$ structures	
	Space	E_{ref}	rms	max	rms	max	rms	max
(a)	Real	0	10.24	21.93	1.09	2.95	2.14	5.44
(b)	Real	$\Omega x(1-x)$	6.51	13.36	1.03	3.05	1.77	4.40
(c)	Recip.	$\Omega x(1-x)$	3.94	8.78	0.74	1.80	1.29	2.67
(d)	Recip.	ΔE_{CS}	1.08	2.33	0.70	1.42	0.82	2.22

three CE's (a)-(c) fails to predict the energies of the longer period superlattices. We will fix this problem next.

C. Treating Long-Period Superlattices

As shown in Figs. 23 and 24, the CE fails to predict the energies of coherent lattice-mismatched superlattices—even for periods as short as $p = 3$. We explained in the previous section that the cause of this problem is the long range coherent relaxation that occurs to relieve the lattice-mismatch-induced strain. In fact, this superlattice problem is caused by a singularity in $J(\vec{k})$ at $\vec{k} = 0$, so that no finite real space expansion will predict the correct limit. It is possible, however, to get the correct long-period superlattice limit if we rewrite the reciprocal space interaction energies as

$$J(\vec{k}) = J_{CS}(\vec{k}) + J_{SR}(\vec{k}), \quad (40)$$

where the first term on the right-hand side is singular at $\vec{k} = 0$, and contains the correct long-period superlattice limit, i.e., the constituent-strain (CS) energy. The continuous part J_{SR} describes the short-ranged (SR) interactions that are ignored by J_{CS} . We will subtract the constituent-strain energy from E_{direct} and determine J_{SR} by fitting to the right hand side of

$$E_{direct}(\sigma) - N \sum_{\mathbf{k}} J_{CS}(\vec{k}) |S(\vec{k}, \sigma)|^2 = N \sum_{\mathbf{k}} J_{SR}(\vec{k}) |S(\vec{k}, \sigma)|^2 + N \sum_{\mathbf{F}}' D_{\mathbf{F}} J_{\mathbf{F}} \bar{\Pi}_{\mathbf{F}}(\sigma). \quad (41)$$

The division into J_{CS} and J_{SR} is somewhat arbitrary; the essential feature is that J_{CS} contain the singularity at the origin, leaving a smooth function J_{SR} , that can be fitted using the techniques of the previous section. Since $J_{CS}(\vec{k})$ is singular at $\vec{k} = 0$, the corresponding real-space pair expansion has an infinite number of non-zero pair interactions.

We have previously shown [70] that $J_{CS} = \Delta E_{CS}^{eq}(\hat{k}, x) / [4x(1-x)]$ can be obtained analytically from continuum elasticity theory as

$$J_{CS}(\hat{k}, x) = \frac{1}{4} \frac{q_A(\hat{k}) q_B(\hat{k}) \Delta E_A(a_B) \Delta E_B(a_A)}{(1-x)q_A(\hat{k}) \Delta E_A(a_B) + xq_B(\hat{k}) \Delta E_B(a_A)}. \quad (42)$$

Here, $\Delta E_A(a_B)$ is the excess energy of *cubic* A deformed hydrostatically to the lattice constant a_B of pure B; an analogous quantity for B-on-A is given by $\Delta E_B(a_A)$. The quantity $q_A(\hat{k})$ is the "epitaxial strain reduction factor" [71]. Its general form is [30,73]:

$$q(\hat{k}) = 1 - \frac{B}{C_{11} + \gamma(\hat{k})\Delta}, \quad (43)$$

where B is the bulk modulus, $\Delta = C_{44} - (C_{11} - C_{12})/2$ is the elastic anisotropy, and γ is a purely geometrical factor given by

$$\gamma(\hat{k}) = \gamma(\phi, \theta) = \sin^2 2\theta + \sin^4 \theta \sin^2 2\phi, \quad (44)$$

where ϕ and θ are spherical polar coordinates defined by $r = [r \sin\theta \cos\phi; r \sin\theta \sin\phi; r \cos\theta]$. For the principal directions we have $\gamma[001] = 0$; $\gamma[011] = 1$, and $\gamma[111] = 4/3$, which is its maximum value. The practical calculation steps are:

(a) Use the LDA to calculate the energies of cubic A at the lattice constant of cubic B [$\Delta E_A(a_B)$] and of B at the lattice constant of A [$\Delta E_B(a_A)$].

(b) Determine $q_A(\hat{k})$ and $q_B(\hat{k})$ by calculating within the LDA the energies of A constrained *epitaxially* to a_B in the plane perpendicular to \hat{k} and relaxed along the \hat{k} direction [$\Delta E_A^{epi}(\hat{k}, a_B)$], and similarly for B on A [$\Delta E_B^{epi}(\hat{k}, a_A)$]. This is repeated for two directions \hat{k} , and the values can then be used to solve for B/C_{11} and Δ/C_{11} for A using $q_A(\hat{k}) = \Delta E_A^{epi}(\hat{k}, a) / \Delta E_A(a)$, and similarly for B. The added work required relative to the regular CE is quite small since each calculation is for the basic unit cell of the lattice, containing only one or two atoms.

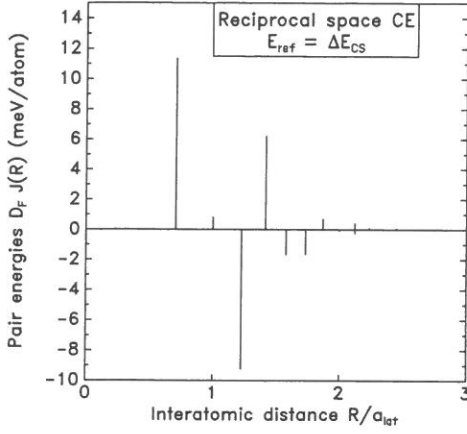


Figure 26. Real-space pair interaction energies of GaP/InP from the reciprocal space fit using input set s_2 and $E_{\text{ref}} = \Delta E_{\text{CS}}^{\text{eq}}(\hat{k}, x)$. From ref [70].

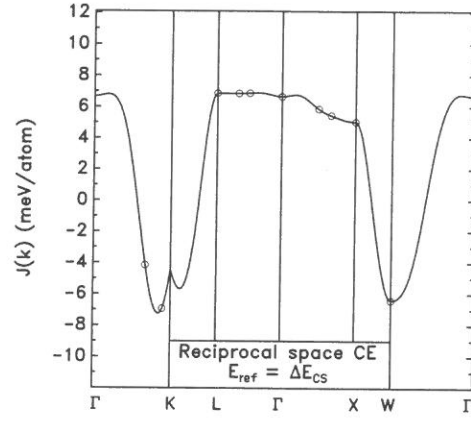


Figure 27. $J(\vec{k})$ of GaP/InP along the principal directions in the Brillouin Zone for the same CE described in Fig. 26. From ref [70].

(c) Evaluate $J_{\text{CS}}(\hat{k}, x)$ using Eq. (42) and use Eq. (45) to perform the cluster expansion:

$$\sum_{\sigma' \in s} \omega_{\sigma'} \left[E_{\text{direct}}(\sigma') - \sum_k J_{\text{CS}}(\hat{k}, x) |S(\vec{k}, \sigma')|^2 - E'_{\text{CE}}(\sigma') \right]^2 + tM = \text{Minimum}, \quad (45)$$

where E'_{CE} is defined by the r.h.s. of Eq. (36). The CE prediction for the $E_{\text{direct}}(\sigma)$ is

$$E_{\text{CE}}(\sigma) = E'_{\text{CE}}(\sigma) + N \sum_k J_{\text{CS}}(\hat{k}, x) |S(\vec{k}, \sigma)|^2. \quad (46)$$

D. Tests of the Reciprocal Space Cluster Expansion with the Constituent Strain Term

We now present the results for the procedure outlined above. This CE differs from that of Fig. 25c only in that we subtract from the directly-calculated energies the quantity $E_{\text{ref}} = E_{\text{CS}}^{\text{eq}}(\hat{k}, x)$ in place of $E_{\text{ref}} = \Omega x(1 - x)$. The prediction errors from this CE are shown in Fig. 25(d), and the real space pair interactions and $J(\vec{k})$ (excluding J_{CS}) for this CE are shown in Figs. 26 and 27, respectively. Figure 28 shows that, as promised, the new fit solves the long-period superlattice problem demonstrated in Fig. 23. As before, we test the CE by predicting the energies of three sets of new structures, the long-period superlattices, swapped short-period

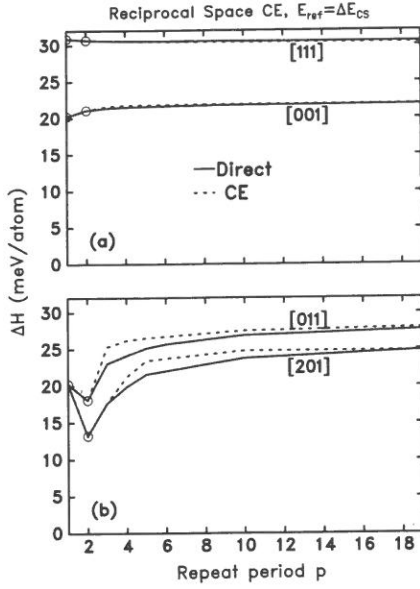


Figure 28. Formation energies for GaP/InP superlattices as a function of repeat period, p . Solid lines are results calculated with the VFF model. Dashed lines are results of a CE of Eq. (45). The set of structures used to fit the interaction energies contains only structures with $p \leq 2$. From ref [70].

structures, and $x \neq 1/2$ structures. These results are shown in the last line of Table IV. Comparing parts (c) and (d) of Fig. 25, we find that the predictions for the long-period superlattices are of course, greatly improved. But we also find better predictions for the swapped structures. *This shows that the form that we use for J_{CS} is also helpful for short-period structures.* Hence, the CE of Eqs. (41)-(46) should be generally applicable, replacing the conventional real space methods.

We can also use this CE to predict the energy of the random GaP/InP alloy. For the CE prediction of the random alloy energy for $x = 1/2$, we average $\Delta E_{CS}^{eq}(\hat{k}, x = 1/2)$ over all solid angles. (This involves a slight approximation, as we should really be averaging over the first Brillouin Zone.) We write

$$E_{CE}(\text{random}) = J_0 + \int \Delta E_{CS}^{eq}(\hat{k}, x) d\hat{k} \quad (47)$$

The angular average of ΔE_{CS}^{eq} is 27.16 meV/atom and $J_0 = -6.47$ meV/atom. The CE predicted energy is 20.69 meV/atom, compared with 20.45 meV/atom from direct calculations [72].

We expect that our reciprocal-space cluster expansion will open the way to accurate, first-principles calculations of systems with significant size-mismatch. We have applied it to the Cu-Pd system in the fcc structure, using the LAPW-calculated formation enthalpies discussed in Sec. VIII. We find a reasonably good fit and small prediction errors. We are applying the simulated annealing method to the reciprocal-space cluster expansion to find ground state structures and predict diffuse scattering profiles.

XI. OTHER APPLICATIONS

We close this review by noting other applications of the cluster expansion.

A. Surface Thermodynamics

It is possible to apply the cluster expansion formalism to *surface* thermodynamics by replacing the calculated *bulk* energies of Eq. (5) with *surface* formation energies [74]. The latter calculations involve both surface relaxation and surface reconstructions. Application to the $\text{Ga}_{0.5}\text{In}_{0.5}\text{P}/\text{GaAs}$ (001) surface shows that the CuPt-surface contains homopolar Ga-Ga and In-In dimers, whereas the chalcopyrite surface (Fig. 29) exhibits heteropolar dimers [75]. Relative to the undimerized surfaces, dimerization lowers the energy by an average of 600 meV per surface atom. In addition to dimerization (Fig. 29b) we find in all cases two other energy-lowering reconstructions within the 2×2 surface unit cell. First, dimers relax perpendicularly to the surface creating $[\bar{1}10]$ dimer rows of alternating high and low dimers (see Fig. 29c). We will refer to this as "buckling". Second the high dimer tilts in the $[110]$ direction becoming nonhorizontal, whereas the low dimer remains virtually horizontal [Fig. 29(d)]. This tilt is natural for surfaces with heteropolar dimers, but constitutes a symmetry breaking for the other surfaces. Since the four surface sites are inequivalent in the final geometry, there are two different ways of distributing the two Ga and the two In atoms in each of the topologies. We will characterize this by the type of atom (Ga or In) occupying the site on the high dimer that tilts upwards. We find that the CuPt-surface strongly prefers having the larger In atom on the high dimer, whereas the chalcopyrite surface shows a slight preference for the smaller (but more electronegative) Ga atom to be tilted up. Tilting leads to a uniform energy lowering of 100 meV but does not affect the relative stability of the surfaces.

We find that the reconstructions (dimerization, buckling, and tilting) considerably lower the energy of all the surfaces and, most significantly, make the surface corresponding to the observed CuPt ordering the lowest in energy by 84 meV per surface atom. Thus, surface reconstruction not only favors atomic arrangements that are unstable in the bulk (see the CP = CuPt bulk energy in Fig. 11b), but it also results in energy differences large enough to produce order at growth temperature.

At finite temperatures, the thermodynamics of the unreconstructed and the 2×2 reconstructed surfaces is obtained by minimizing the free energy with respect to the average spin products $\bar{\Pi}_{\mathbf{F}}(\sigma)$. For the unreconstructed surface we use the model of an anisotropic square lattice (equivalent to the rectangular lattice), while for the reconstructed surface we use the model

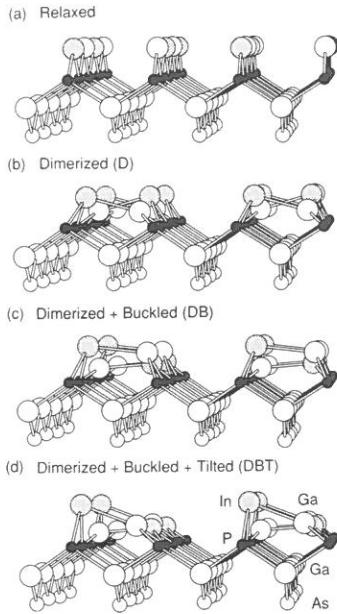


Figure 29. Side view of atomic geometries for the various reconstruction modes described in the text for the cation terminated chalcopyrite surface of GaInP_2 . The atoms for Ga (white), In (grey), and P (black) on top of a (001) substrate GaAs layer (white).

of $2 \times \infty$ independent rows. The square approximation of the CVM [11] was used to get the thermodynamics in both cases.

Minimization of the Hamiltonian produces the $T = 0$ ground-state energy as a function of composition x . For both the unreconstructed and reconstructed cation-terminated top surfaces we find that the CuPt_B structure is the ground state at $x = 1/2$. To see if the energy differences between different surface structures are sufficient to preserve any type of order at typical growth temperatures, we calculated the CuPt order parameter η_B , defined as

$$\eta_B(T) = \frac{1}{2} |c_\alpha + c_\beta - c_\gamma - c_\delta|, \quad (48)$$

as a function of temperature, where C_γ are the In occupation probabilities on the four sublattices γ . For the CuPt structure, perfect ordering gives

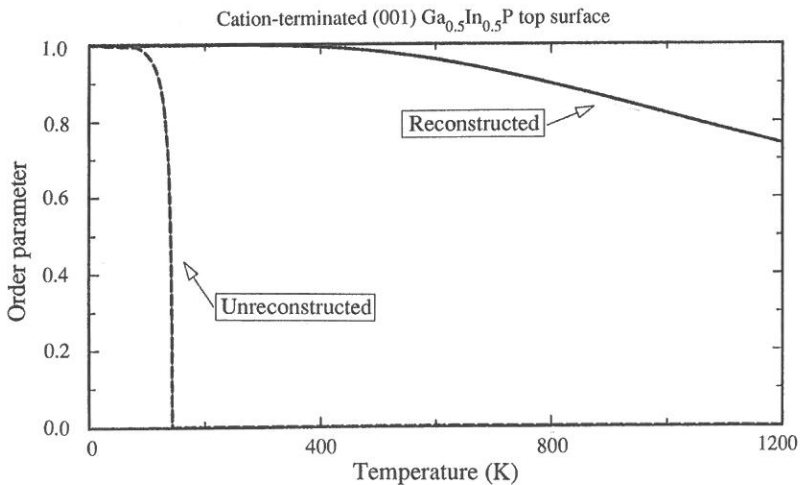


Figure 30. Calculated CuPt long range order parameter η [Eq. (48)] for the cation-terminated $\text{Ga}_{0.5}\text{In}_{0.5}\text{P}$ (001) surface. Note how reconstruction eliminates the low-temperature critical transition, replacing it by a continuous transition in which significant ordering exists even at growth temperature (~ 900 K). From ref [76].

$\eta = 1$. Figure 30 displays the CVM results for $\eta(T)$, of the cation-terminated surface. For the *unreconstructed* case, the system undergoes a phase transition to the disordered phase at $T_c = 146$ K. It is clear that at growth temperatures (typically 900 K) no traces of long-range CuPt_B ordering are to be expected with an unreconstructed surface. For the *reconstructed* case, on the other hand, *there is no phase transition*. However, the CuPt_B order parameter η_B [Eq. (48)] is seen to be significant at growth temperatures (e.g., $\eta_B = 0.87$ at $T = 900$ K.) This order parameter approaches zero only asymptotically as $T \rightarrow \infty$.

To summarize, the CE can be used to understand also surface thermodynamics. For III-V semiconductors we discover that surface reconstruction stabilizes even at growth temperatures a bulk-unstable ordered structure that is observed experimentally [74].

B. Ternary Systems

Many interesting alloys exhibit competition of *three* atomic species on the same lattice. Semiconductor examples include the technologically-important (in solar cells) $(\text{CuInSe}_2)_x$ $(\text{ZnSe})_{2x}$ system in which Cu, In, and Zn can reside on the fcc lattice. More generally, we have an alloy of $\text{A}_{1-x}\text{B}_x\text{C}$ with DC. We will address here the $x = 1/2$ problem. The statistical mechanics [76] was addressed in two steps. First, we consider the occupations of the fcc cation sublattice by A and B atoms in the $\text{A}_{0.5}\text{B}_{0.5}\text{C}^{\text{VI}}$ system. Second, we add the third cation D^{II} competing for the same sublattice. The common anion C resides on its own fcc sublattice and hence does not carry a statistical degree of freedom. (We neglect high-energy anion-cation anti-site defects.) In addressing the first problem we consider the spin-1/2 Ising model where site i is occupied by either an A atom ($\sigma_i = -1$) or by a B atom ($\sigma_i = +1$). We take the Ising Hamiltonian for an arbitrary configuration $\vec{\sigma}$ of this binary system to be

$$H_{\text{bin}}(\vec{\sigma}) = \tilde{J}_0 \sum_{(ij)} J_{ij} \sigma_i \sigma_j + \sum_{(ijkl)} J_{ijkl} \sigma_i \sigma_j \sigma_k \sigma_l, \quad (49)$$

where (ij) indicates a summation over all pairs, and $(ijkl)$ indicates a summation over all tetrahedra in the lattice. To find the values of the interaction parameters $\{J\}$ we fit Eq. (49) to a set of directly calculated LDA formation enthalpies $\Delta H(\sigma)$ of simple AC/BC ordered structures at the equilibrium volume. We have used LDA to calculate $\Delta H(\sigma)$ for six equimolar $(\text{CuSe})_p(\text{InSe})_p$ short-period ($p = 1, 2$) superlattices, not including the chalcopyrite structure. Retaining in Eq. (49) only the empty-site energy \tilde{J}_0 and the nearest-neighbor pair interaction J_2 produces a prediction of $\Delta H_f(\text{CH}) = -1183.4$ meV/cation compared with the LDA value $\Delta H_f(\text{CH}) = -1163.0$ meV/cation. This 20 meV prediction error can be reduced to 0.4 meV

if the nearest-neighbor four-body term J_4 is added. Further addition of second-, third-, and fourth-neighbor pair interactions J_{ij} lead to a similar prediction error of 0.25 meV. We thus choose to retain only \tilde{J}_0 , J_2 , and J_4 in the Hamiltonian of Eq. (49). The order-disorder transition obtained in a Monte-Carlo (MC) simulation for CuInSe_2 [8e] is $T_c = 1120$ K, in perfect agreement with the result using up to fourth-neighbor pair interactions (the experimental result is [8e] 1083 K). The CVM tetrahedron approximation leads to $T_c = 1224$ K. The four-body term J_4 acts to lower T_c by as much as 300 K in both the MC and the CVM calculation. We will hence proceed using CVM with the fitted interaction energies given above.

The consideration of the pseudoternary case $(\text{ABC}_2)_{1-x}(\text{DC})_{2x}$ requires two changes. First, a generalization to a spin-1 Hamiltonian, representing occupations of site i by A ($S_i = 1$), B ($S_i = -1$), and D ($S_i = 0$) is needed. Second, the added interaction terms are now *volume-dependent* since the end-point chalcopyrite and zincblende constituents can have different equilibrium molar volumes, in contrast to the pseudobinary case, where all structures $(\text{CuSe})_p(\text{InSe})_p$ had the same composition and, hence, nearly equal molar volumes. We will therefore use a nearest-neighbor spin-1 Ising model (a generalized Blume-Emery-Griffiths [77], or BEG model) with volume-dependent interactions:

$$H_{\text{tern}}(S, V) = \left[J_2 \sum_{\langle ij \rangle} S_i S_j + J_4 \sum_{\langle ijkl \rangle} S_i S_j S_k S_l \right] + J_0(V) + D(V) \sum_i S_i^2 - K(V) \sum_{\langle ij \rangle} S_i^2 S_j^2. \quad (50)$$

The terms in brackets are the nearest-neighbor terms of Eq. (49). All odd terms [77] were omitted, assuming that the Hamiltonian is invariant under the $A \leftrightarrow B$ interchange.

Using the LAPW method we have calculated the volume-dependent total energies E_S for structures $S = \text{ZB}$, CH , and stannite ST , finding also the equilibrium volumes V_S . Interpolating these volumes we get $V(x)$. The functions $J_0[V(x)]$, $D[V(x)]$, and $K[V(x)]$ are then obtained by fitting Eq. (50) to the three LAPW equations of state $E_S(V)$, keeping J_2 and J_4 constant at their values in $\text{A}_{0.5}\text{B}_{0.5}\text{C}$.

We solved the statistical mechanics of Eq. (50) in the CVM tetrahedron approximation. Statistical correlations inside the tetrahedron cluster are correctly described, but longer-range correlations, present in MC simulations, are neglected. We have therefore scaled down our CVM temperature approximately by $T_{\text{MC}}/T_{\text{CVM}} = 0.92$, obtained from MC and CVM calculations on the pseudobinary $\text{A}_{0.5}\text{B}_{0.5}\text{C}$ system (including both J_2 and J_4). At each composition and temperature, the CVM free energy $F = H_{\text{tern}} - TS$ is minimized with respect to the occupation variables, using the "natural iteration" [11] procedure, and with respect to the molar volume V .

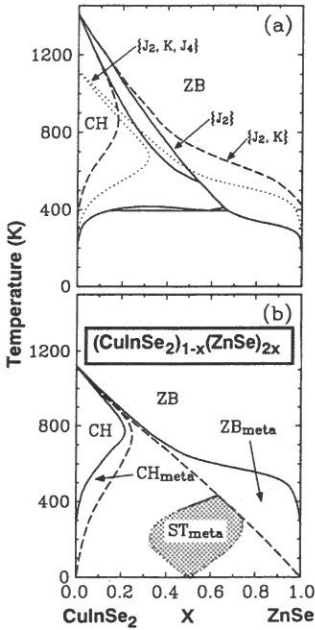


Figure 31. Calculated phase diagram of $\text{CuInSe}_2/\text{ZnSe}$ using a few representations: (a) J_2 -only; $J_2 + K_2$; $J_2 + K_2 + J_4$. In (b) we show the result including volume-dependent interaction energies. From Ref. [76].

Figure 31 shows the calculated phase diagrams of $(\text{CuInSe}_2)_{1-x}(\text{ZnSe})_{2x}$, using a hierarchy of approximations in the Hamiltonian of Eq. (50): (i) J_2 only (ii) J_2 and K (iii), J_2 , K and J_4 (iv) volume-dependent interaction-energies. In cases (ii) and (iii) we used the value $\tilde{K} \equiv K + g(V_{\text{ST}})/2 = 10.5$ meV for K , corresponding to a fit of the BEG Hamiltonian to the equilibrium-volume energies of the CH, ST, and ZB structures. The diagram of case (i) corresponds to the antiferromagnetic spin-1 Ising model in the fcc sublattice. The diagram of case (ii) shows the role of positive K values: it widens the CH-ZB miscibility gaps, suppressing the small second-order transition line present in case (i) between ≈ 410 and 550 K, and removes the triple point. The diagram of case (iii) shows that J_4 acts to reduce considerably the transition temperatures in the low- x region and to reduce the width of the CH-ZB miscibility gap. Finally, the use of volume-dependent interactions acts to increase the CH-ZB miscibility gap

[Fig. 31(b)]. The maximum equilibrium solubility of ZnSe in CuInSe_2 with the chalcopyrite structure is 22% (at $T \approx 770$ K), while CuInSe_2 becomes completely soluble in ZnSe with the zinc-blend structure above the order-disorder temperature of CuInSe_2 . Our results hence show that, contrary to the other known heterostructural ternary alloy $(\text{GaAs})_{1-x}\text{Ge}_{2x}$, characterized by vanishing solid solubility, $(\text{CuInSe}_2)_{1-x}(\text{ZnSe})_{2x}$ should exhibit substantial miscibility. Additional metastable features are presented for this *ab initio* phase diagram. The left dashed line in Fig. 31(b) marks the chalcopyrite spinodal, which is the upper-composition limit of metastability for the CH phase. The right dashed line is the unstable second-order transition line inside the coexistence region and marks the lower-composition limit for metastability of the zinc-blende phase. Between these two lines we find $\partial^2 F / \partial x^2 < 0$, which implies that any incipient phase separation will be preferred to a single-phase state. Since at $x = 1/2$ we found $0 < \Delta H(\text{ST}) < \Delta E_{\text{VD}} < \Delta E_{\text{Rand}}$, the stannite structure could be observed in $(\text{CuInSe}_2)_{1-x}(\text{ZnSe})_{2x}$ if *long-range* atomic diffusion were inhibited. The shaded region at $x \sim 1/2$, $T < 440$ K shows this marginally *metastable ST* phase. It should be observed if *short-range* atomic rearrangements are allowed but *long-range* atomic migration (and hence, phase separation) is slow at $T < 440$ K. The

chalcopyrite-forbidden x-ray diffraction peaks at (001), (110), (112), and (221) $2\pi/a$ characterize the ST phase. Calorimetric and magnetic-susceptibility measurements in $(A^I B^{III} Te_2)_{1-x} (MnTe)_{2x}$ alloys have indicated two low-temperature phases described by ordering of the Mn atoms. Although the structure of these phases is still unknown (the above mentioned x-ray peaks were not measured) the structure called "chalcopyrite-ordered" could be stannite-like.

XII. SUMMARY

We have shown how total energy LDA calculations of O(10) ordered structures can be used to extract the "building blocks" interaction energies $\{J_F\}$, and how these can be used in conjunction with lattice statistical mechanics techniques to calculate thermodynamic properties. The quantities that can be calculated in this way include: (i) identification of the $T = 0$ lowest energy configuration out of 2^N possibilities, (ii) formation energies of "complex" structures, not amenable to *direct* LDA calculations, (iii) excess configurational enthalpies, entropies, and free energies as a function of (x,T) , (iv) composition-temperature phase diagrams, (v) SRO and LRO parameters as a function of (x,T) , and (vi) equilibrium lattice constants, interatomic distances, and elastic constants as a function of (x,T) . The systems for which the method has been illustrated include (a) pseudobinary $A_{1-x} B_x C$ semiconductor alloys, (b) binary $A_{1-x} B_x$ transition metal alloys, (c) Ternary alloys such as $CuInSe_2/ZnSe$, (d) epitaxial phase diagrams, and (e) surface phase diagrams. The main advantages of this method lie in its ability to predict unsuspected structures and to *analyze* trends in the above quantities in terms of electronic structure constructs, thus helping to demystify the highly successful Pauling-esque rules of metallurgy and structural solid-state chemistry. Its main drawback is that in the presence of relaxation, it requires LDA calculations on a significant number (10-20) of ordered structures. Its main distinguishing feature relative to the coherent potential approximation based methods (e.g., GPM, CW) is that charge, potential and relaxational fluctuations are included at the outset in a non-perturbative fashion and that the mean-field approximation is avoided. Consequently, our method is capable of treating complex, low-symmetry atomic configurations with a similar degree of accuracy currently afforded by LDA calculations on ordered crystals.

Acknowledgments

It is a pleasure to thank my many collaborators in this field of research J. E. Bernard, L. G. Ferreira, S. Froyen, D. B. Laks, Z. W. Lu, R. Magri, R. Osorio, and S.-H. Wei. This work was supported in part by the U.S. Department of Energy, Office of Energy Research, Basic Energy Science, Division of Materials Science, through grant No. DE-A-CO2-83CH10093.

REFERENCES

1. P. Hohenberg and W. Kohn, *Phys. Rev.* **136**, B864 (1964); W. Kohn and L. J. Sham, *Phys. Rev.* **140**, A1133 (1965); J. T. Devreese and P. Van Camp, *Electronic Structure, Dynamics and Quantum Structural Properties of Condensed Matter*, NATO series vol. **121** (Plenum Press, New York, 1986).
2. A. Bieber and F. Gautier, *Acta Metall.* **34**, 2291 (1986).
3. C. R. A. Catlow and W. C. Mackrodt, *Computer Simulations in Solids* (Springer-Verlag, Berlin 1982); I. M. Torrence, *Interatomic Potentials* (Academic, New York, 1972); S. M. Foiles, *Phys. Rev. B* **32**, 7685 (1985); P. C. Kelires and J. Tersoff, *Phys. Rev. Lett.* **63**, 1164 (1989).
4. C. Domb in *Phase Transitions and Critical Phenomena*, edited by C. Domb and H. S. Green (Academic, London, 1974), Vol. **3**, p. 358.
5. D. de Fontaine in *Solid State Physics*, edited by H. Ehrenreich, F. Seitz, and D. Turnbull (Academic, New York, 1979), Vol. **34**, p. 73.
6. J. M. Sanchez and D. de Fontaine in *Structure and Bonding in Crystals*, edited by M. O'Keefe and A. Navrotsky (Academic, New York, 1981), Vol. **2**, p. 117.
7. J. W. D. Connolly and A. R. Williams, *Phys. Rev. B* **27**, 5169 (1983).
8. (a) L. G. Ferreira, S.-H. Wei, and A. Zunger, *Phys. Rev. B* **40**, 3197 (1989); (b) S.-H. Wei, L. Ferreira and A. Zunger, *Phys. Rev. B* **41**, 8240 (1990). (c) R. G. Dandrea, J. E. Bernard, S.-H. Wei, and A. Zunger, *Phys. Rev. Lett.* **64**, 36 (1990). (d) A. A. Mbaye, L. G. Ferreira, and A. Zunger, *Phys. Rev. Lett.* **58**, 49 (1987); (e) S.-H. Wei, L. G. Ferreira, and A. Zunger, *Phys. Rev. B* **45**, 2533 (1992).
9. J. M. Sanchez, F. Ducastelle, and D. Gratias, *Physica A* **128**, 334 (1984).
10. J. Kanamori and Y. Kakehashi, *J. Physique* **38**, 274 (1977); F. Ducastelle, *Order and Phase Stability in Alloys* (North Holland, Amsterdam, 1991).
11. R. Kikuchi, *J. Chem. Phys.* **60**, 1071 (1974); *Phys. Rev.* **81**, 988 (1951).
12. N. Metropolis, A. W. Rosenbluth, M. V. Rosenbluth, A. Teller and E. Teller, *J. Chem. Phys.* **60**, 1071 (1974).
13. R. Magri, J. E. Bernard, and A. Zunger, *Phys. Rev. B* **43**, 1593 (1991).
14. Z. Xi, B. Chakraborty, K. W. Jacobsen, and J. Norskov, *J. Phys. Condens. Matter* **4**, 7191 (1992); B. Chakraborty and Z. Xi, *Phys. Rev. Lett.* **68**, 2039 (1992).
15. R. Kikuchi, J. M. Sanchez, D. de Fontaine, and H. Yamaguchi, *Acta Metall.* **28**, 651 (1980); J. M. Sanchez, J. R. Barefoot, R. N. Jarrett, and J. K. Tien, *Acta Metall.* **32**, 1519 (1984).
16. C. Sigli and J. M. Sanchez, *Acta Metall.* **33**, 1097 (1985).
17. L. G. Ferreira, A. A. Mbaye, and A. Zunger, *Phys. Rev. B* **37**, 10547 (1988).
18. S. de Gironcoli, P. Giannozzi, and S. Baroni, *Phys. Rev. Lett.* **66**, 2116 (1991).
19. F. Ducastelle and F. Gautier, *J. Phys. F* **6**, 2039 (1976).
20. M. Sluiter and P. E. A. Turchi, *Phys. Rev. B* **40**, 11215 (1989).
21. C. Sigli and J. M. Sanchez, *Acta Metall.* **36**, 367 (1988).
22. B. L. Gyorffy and G. M. Stocks, *Phys. Rev. Lett.* **50**, 374 (1983).
23. D. D. Johnson, D. M. Nicholson, F. J. Pinski, B. L. Gyorffy, and G. M. Stocks, *Phys. Rev. Lett.* **56**, 2088 (1986).
24. G. P. Srivastava, J. L. Martins, and A. Zunger, *Phys. Rev. B* **31**, 3561 (1985).
25. K. Terakura, T. Oguchi, T. Mohri, and K. Watanabe, *Phys. Rev. B* **36**, 2169 (1987).

26. J. M. Sanchez, *Solid State Commun.* **65**, 527 (1988).
27. A. E. Carlsson, *Phys. Rev. B* **40**, 912 (1989).
28. Z. W. Lu, S.-H. Wei, A. Zunger, S. Frota-Pessoa, and L. G. Ferreira, *Phys. Rev. B* **44**, 512 (1991); L. G. Ferreira, S.-H. Wei, and A. Zunger, *Int. J. Supercomputer Applic.* **5**, 34 (1991).
29. Z. W. Lu, S.-H. Wei, and A. Zunger, *Phys. Rev. Lett.* **68**, 1961 (1992).
30. Z. W. Lu, S.-H. Wei, and A. Zunger, *Phys. Rev. B* **45**, 10314 (1992); *ibid* **44**, 3387 (1991).
31. R. Magri, S.-H. Wei, and A. Zunger, *Phys. Rev. B* **42**, 11388 (1990).
32. R. Magri and A. Zunger, *Phys. Rev. B* **44**, 8672 (1991).
33. W. H. Press, B. P. Flannery, S. A. Teukolsky, and W. T. Vetterling, *Numerical Recipes* (Cambridge University Press, Cambridge, 1986).
34. (a) G. M. Stocks and H. Winter, in *Electronic Structure of Complex Systems*, p. 463, edited by P. Phariseau and W. M. Temmerman (Plenum Press, NY, 1984); (b) Local environment effects were discussed by M. Yu. Nikolaev, L. M. Roth, and A. V. Vedyayev, *Phys. Rev. B* **46**, 7358 (1992).
35. I thank S. Baroni for insightful correspondence on this point.
36. P. P. Ewald, *Ann. Phys. (NY)* **64**, 253 (1921).
37. L. M. Foster et al., *J. Electrochem. Soc.* **119**, 765 (1972); V. T. Bublik and V. N. Leikin, *Phys. Stat. Solidi A* **46**, 365 (1978).
38. D. M. Wood, *J. Vac. Sci. Technol.* **10B**, 1675 (1992).
39. (a) M. Cyrot and F. Cyrot-Lackmann, *J. Phys. F* **6**, 2257 (1976); (b) M. Sluiter, P. Turchi, and D. de Fontaine, *ibid* **17**, 2163 (1987); (c) J. Van Der Rest, F. Gautier, and F. Brouers, *ibid* **5**, 2283 (1975).
40. D. G. Pettifor, *Phys. Rev. Lett* **42**, 846 (1979).
41. G. Treglia and F. Ducastelle, *J. Phys. F* **17**, 1935 (1987).
42. P. M. Hansen, *Constitution of Binary Alloys* (McGraw-Hill, New York, 1958).
43. T. B. Massalski, *Binary Alloy Phase Diagrams* (American Society for Metals, Metals Park, OH, 1986).
44. C. E. Dahmani, et al., *Phys. Rev. Lett.* **55**, 1208 (1985).
45. E. Raub, *J. Less. Common Met.* **1**, 3 (1959).
46. J. B. Darby and K. M. Myles, *Metallurg. Transact.* **3**, 653 (1972).
47. A. Kidron, *Phys. Lett* **25A**, 112 (1967).
48. S.-H. Wei and H. Krakauer, *Phys. Rev. Lett.* **55**, 1200 566 (1985).
49. (a) J. E. Shield and R. K. Williams, *Scripta Metall.* **21**, 1475 (1987); (b) E. Raub, H. Beeskow, and D. Menzel, *Z. Metallk.* **50**, 428 (1959).
50. P. E. A. Turchi, et al., *Phys. Rev. B* **37**, 5982 (1988).
51. Z. W. Lu, S.-H. Wei and A. Zunger, *Europhys. Lett.* **21**, 221 (1993).
52. F. J. Pinski, B. Ginatempo, D. D. Johnson, J. B. Staunton, G. M. Stocks, and B. L. Gyorffy, *Phys. Rev. Lett.* **66**, 766 (1991).
53. P. A. Flinn, B. L. Averbach, and M. Cohen, *Acta. Metall* **1**, 664 (1953); J. E. Woodilla and B. L. Auerbach, *ibid* **16**, 255 (1963).
54. *Binary Alloy Phase Diagrams*, edited by J. L. Murray, L. H. Bennett, and H. Barker (American Society of Metals, Metals Park, OH, 1986).
55. W. G. Moffatt, *The Handbook of Binary Phase Diagrams* (Gernium, Schenectady, NY, 1984).

56. R. Hultgren, P. D. Desai, D. T. Hawkins, M. Gleiser, and K. K. Kelley, *Selected Values of the Thermodynamics Properties of Binary Alloys* (American Society for Metals, Metals Park, OH, 1973).
57. (a) *Phase Diagrams of Binary Gold Alloys*, edited by H. Okamoto and T. B. Massalski (ASM International, Materials Park, OH, 1987); (b) P. D. Desai, *J. Phys. Chem. Ref. Data* **16**, 109 (1987).
58. A. Schneider and U. Esch, *Z. Elektrochem.* **50**, 290 (1944).
59. M. Sluiter, P. E. A. Turchi, F. J. Pinski, and G. M. Stocks, *Mat. Sci. & Engineering A* **152**, 1 (1992).
60. A. G. Khachaturyan, *Theory of Structural Transformations in Solids* (Wiley, New York, 1983), p. 459.
61. V. G. Vaks, *Phys. Lett.* **163A**, 209 (1992).
62. J. C. Mikkelsen and J. B. Boyce, *Phys. Rev. Lett.* **49**, 1412 (1982).
63. G. Renaud, N. Motta, F. Lancon, and M. Belakhovsky, *Phys. Rev B* **38**, 5944 (1988).
64. J. L. Martins and A. Zunger, *Phys. Rev. B* **30**, 6127 (1984); P. Letardi, N. Motta, and A. Balzarotti, *J. Phys. C* **20**, 2583 (1991); M. Ichimura and A. Sasaki, *Phys. Rev. B* **36**, 9694 (1987).
65. A. E. Carlson and P. J. Meschter, *J. Mater. Res.* **5**, 2813 (1990).
66. R. Magri, S. Froyen and A. Zunger, *Phys. Rev. B* **44**, 7947 (1991); S.-H. Wei and A. Zunger, *ibid.* **43**, 1662 (1991).
67. (a) P. E. A. Turchi, M. Sluiter, F. J. Pinski, D. D. Johnson, D. M. Nicholson, G. M. Stocks, and J. B. Staunton, *Phys. Rev. Lett.* **67**, 1779 (1991); (b) M. Sluiter, D. de Fontaine, X. A. Guo, R. Podloucky, and A. J. Freeman, *Phys. Rev.* **42**, 10460 (1990).
68. A. Sher, M. van Schilfgaarde, A.-B. Chen, and W. Chen, *Phys. Rev. B* **36**, 4279 (1987).
69. P. N. Keating, *Phys. Rev.* **145**, 367 (1966); R. M. Martin, *Phys. Rev. B* **1**, 4005 (1970).
70. D. B. Laks, S. Froyen, L. G. Ferreira, and A. Zunger, *Phys. Rev. B*, **46**, 12587 (1992).
71. A. Zunger and D. M. Wood, *J. Crystal Growth* **98**, 1 (1989).
72. J. E. Bernard (unpublished).
73. S. Froyen, S.-H. Wei, and A. Zunger, *Phys. Rev. B* **38**, 10124 (1988).
74. R. Osorio, J. E. Bernard, S. Froyen and A. Zunger, *Phys. Rev. B* **45**, 11, 173 (1992) *ibid.*, *J. Vac. Sci. Technol.* **10B**, 1683 (1992).
75. S. Froyen and A. Zunger, *Phys. Rev. Lett.* **66**, 2132 (1991); J. E. Bernard, S. Froyen and A. Zunger, *Phys. Rev. B* **44**, 11, 178 (1991).
76. R. Osorio, Z. W. Lu, S.-H. Wei and A. Zunger, *Phys. Rev. B*, **47**, 9985 (1993); S.-H. Wei, L. G. Ferreira and A. Zunger, *Phys. Rev. B* **45**, 2533 (1992); R. Osorio, S. Froyen, and A. Zunger, *Solid State Commun.* **78**, 249 (1991).
77. M. Blume, V. J. Emery and R. B. Griffith, *Phys. Rev. A* **4**, 1071 (1971).

